ACS NANO

www.acsnano.org

Balancing the Nanoscale Organization in Multivalent Materials for Functional Inhibition of the Programmed Death-1 Immune Checkpoint

Kaltrina Paloja,[¶] Jorieke Weiden,[¶] Joschka Hellmeier, Alexandra S. Eklund, Susanne C. M. Reinhardt, Ian A. Parish, Ralf Jungmann, and Maartje M. C. Bastings*

Cite This: *ACS Nano* 2024, 18, 1381−1395

Read Online

ACCESS | Metrics & More | Article Recommendations | Supporting Information

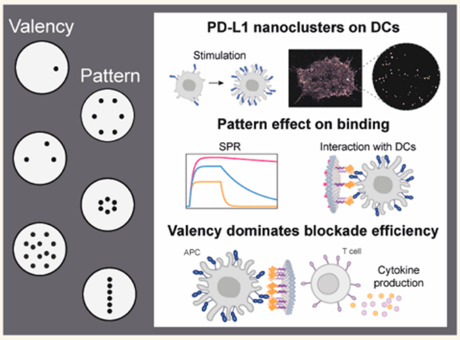

ABSTRACT: **Dendritic cells (DCs) regulate immune priming by expressing programmed death ligand 1 (PD-L1) and PD-L2, which interact with the inhibitory receptor PD-1 on activated T cells. PD-1 signaling regulates T cell effector functions and limits autoimmunity. Tumor cells can hijack this pathway by overexpressing PD-L1 to suppress antitumor T cell responses. Blocking this inhibitory pathway has been beneficial for the treatment of various cancer types, although only a subset of patients responds. A deepened understanding of the spatial organization and molecular interplay between PD-1 and its ligands may inform the design of more efficacious nanotherapeutics. We visualized the natural molecular PD-L1 organization on DCs by DNA-PAINT microscopy and created a template to engineer DNA-based nanoclusters presenting PD-1 at defined valencies, distances, and patterns. These multivalent nanomaterials were examined for their cellular binding and blocking ability. Our data show that PD-1 nano-organization has profound effects on ligand interaction and that the valency of PD-1 molecules modulates the effectiveness in restoring T cell function. This work highlights the power of spatially controlled functional materials to unravel the importance of multivalent patterns in the PD-1 pathway and presents alternative design strategies for immune-engineering.**

KEYWORDS: *spatial organization, dendritic cells, immune checkpoint blockade, DNA origami, multivalency, PD-1, T cell activation*

The programmed cell death protein 1 (PD-1) and its ligands, PD-L1 and PD-L2, are important immune checkpoint regulators that play a critical role in regulating the T cell response during infection and immune tolerance.[1−3] PD-L1/PD-L2 receptors are mainly expressed by antigen-presenting cells (APCs), such as dendritic cells (DCs), while PD-1 is primarily expressed by T cells. When DCs interact with T cells to evoke an antigen-specific immune response, engagement of PD-1 by its ligands PD-L1 and PD-L2 suppresses T cell cytotoxic activity and can induce their apoptosis, thereby balancing the immune response and preventing autoimmunity.[4] However, cancer cells can hijack this homeostatic pathway to evade immune surveillance.[5−7] Cancer cells can suppress T cell activity via upregulation of PD-L1 expression, and thereby restrict immune activation to favor tumor progression. Targeting this regulatory pathway has now become an attractive strategy for cancer immunotherapy.[8−11] Various approaches that exploit monoclonal antibodies targeting PD-1 or its ligands have been developed to block this pathway and have shown great potential in restoring immune function and enhancing antitumor immune responses. Despite promising clinical results, immune therapies face several limitations, including adverse autoimmune events and resistance mechanisms due to heterogeneity of tumors, and only a subset of patients responds to therapy.[12−15] Furthermore, the strong binding interaction between antibodies and their targets obscures a potential nuance in spatial cluster formation as part of active signaling. This motivates a more comprehensive understanding of the complex interplay of the molecules within this pathway to fully seize their implications in cancer therapies.

Received: July 17, 2023
Revised: December 12, 2023
Accepted: December 18, 2023
Published: December 21, 2023

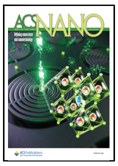

https://doi.org/10.1021/acsnano.3c06552
ACS Nano 2024, 18, 1381−1395

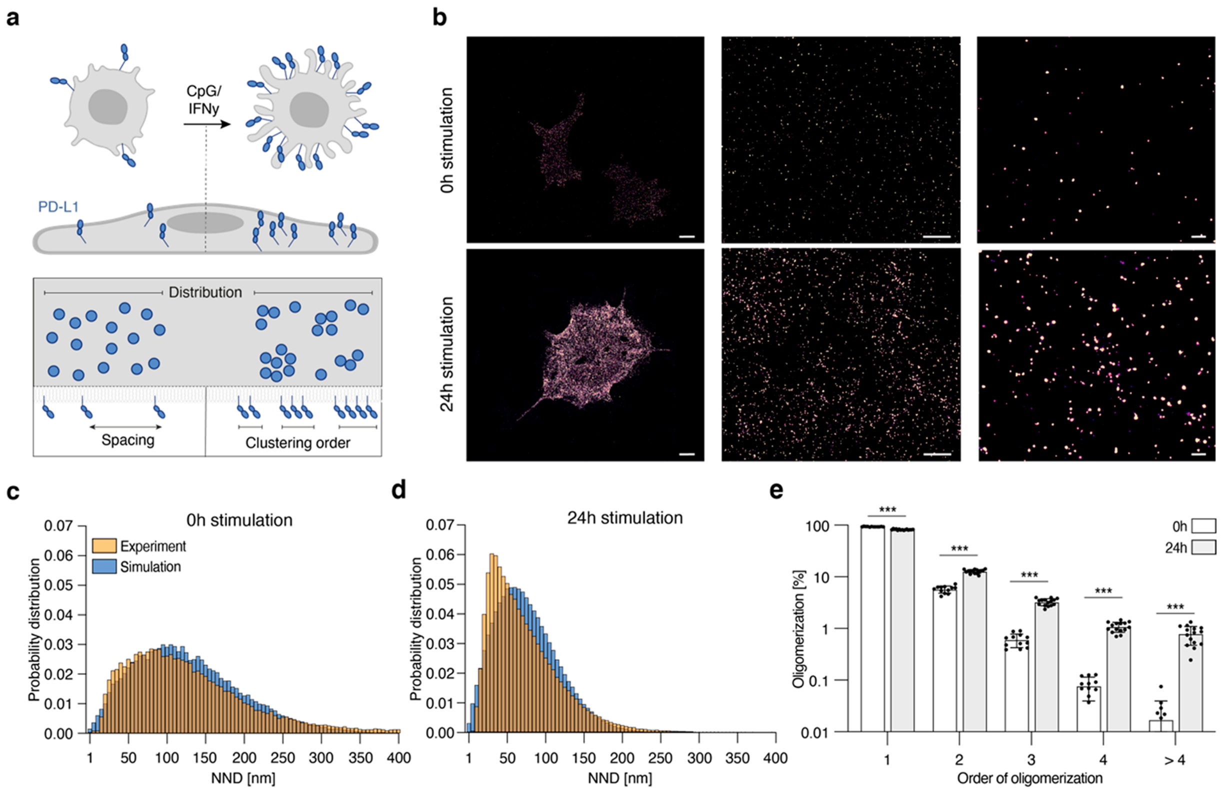

Figure 1. Super-resolution DNA-PAINT imaging of PD-L1 protein on the DC surface. (a) Schematic outline of the parameters that were studied. Change in PD-L1 molecular arrangement between nonactivated DCs and cells stimulated with CpG and IFNγ for 24 h was investigated using DNA-PAINT imaging. Spatial characteristics, including the distribution of PD-L1 (whether random or clustered), inter-PD-L1 spacing, and clustering order, were determined from super-resolved images. (b) DNA-PAINT images of PD-L1 on DCs before (top) and after (bottom) stimulation. Zoom-in images are presented in the middle and on the right. Each spot represents individual PD-L1 molecules. Scale bars = 5 μm, 500 nm, and 100 nm from left to right. (c,d) NND distribution (c) before and (d) after stimulation. Experimental data are highlighted in orange and CSR simulations in blue. (e) Quantitative analysis of the oligomerization order for clusters defined in nonactivated (white) and stimulated (gray) DCs. Error bars indicate SD and statistical analysis was performed using two-tailed Mann−Whitney test (***p < 0.001). Data were derived from two independent experiments and ≥12 cells.

It is now well established that the interaction between T cells and DCs leads to a complex rearrangement of surface proteins, known as the immunological synapse, which physical structure itself impacts the functional response of T cells in various contexts.[16−19] However, the precise details of the spatial organization of immune regulators such as PD-1 or its ligands in this synapse and how it affects T cell function require further investigation. The few studies looking into these parameters have demonstrated that ligand clustering and spatial proximity can have functional consequences on T cell activity. It was shown that PD-1 arranges into inhibitory microclusters on the cell surface of T cells upon binding to PD-L1, promoting inhibition of T cell signaling domains.[20,21] Additionally, PD-1 accumulation at the immunological synapse was found to be dependent on the affinity for its ligands.[22] Similarly, it has been suggested that spatial proximity of PD-L1 ligands may play a role in this inhibitory pathway.[23−25] Despite the limited information, these investigations provide evidence that the spatial organization of PD-1 and its ligands is an important biophysical modulator of T cell function and may have implications for the rational design of immune checkpoint therapies.

Considering the versatile function of DCs in suppressing T cell activity and promoting immune tolerance to maintain homeostasis, we explored how various organizational features of PD-1, such as clustering order, spacing and pattern, affect its interaction with DCs. We capitalized on the high spatial addressability of the DNA origami technology to create nanocontrolled arrays of PD-1.[26−28] This methodology catapulted DNA from its biological context as a source of genetic information by exploiting its material characteristics. The predictable Watson−Crick base pairing affords the engineering of molecular architectures on the nanoscale via self-assembling. In contrast to other available nanoparticles, DNA origami offers perfect control over size, shape, and surface properties guaranteeing uniform particle design. In addition to their inherent biocompatibility, the modulatory properties of nucleic acid-based systems allow the positioning of individual ligand with nanometer precision.[29−34] Benefiting from efforts on structural stabilization and surface characterization, the stability of DNA origami in biological environments as well as interactions with the biointerface are now well understood.[35−37] Together, these features make DNA origami a platform for controlled ligand presentation for receptor binding susceptible to nanoscale ligand presentation.

For the rational design of PD-1 nanoplatforms, we drew inspiration from the natural PD-L1 molecular organization on the DC surface and recapitulated the identified features on DNA origami nanoparticles. To this end, we unveiled key parameters of PD-L1 organization on the DC surface by super-resolution microscopy using DNA-PAINT imaging. We built upon these structural findings to create a library of DNA

https://doi.org/10.1021/acsnano.3c06552
ACS Nano 2024, 18, 1381−1395

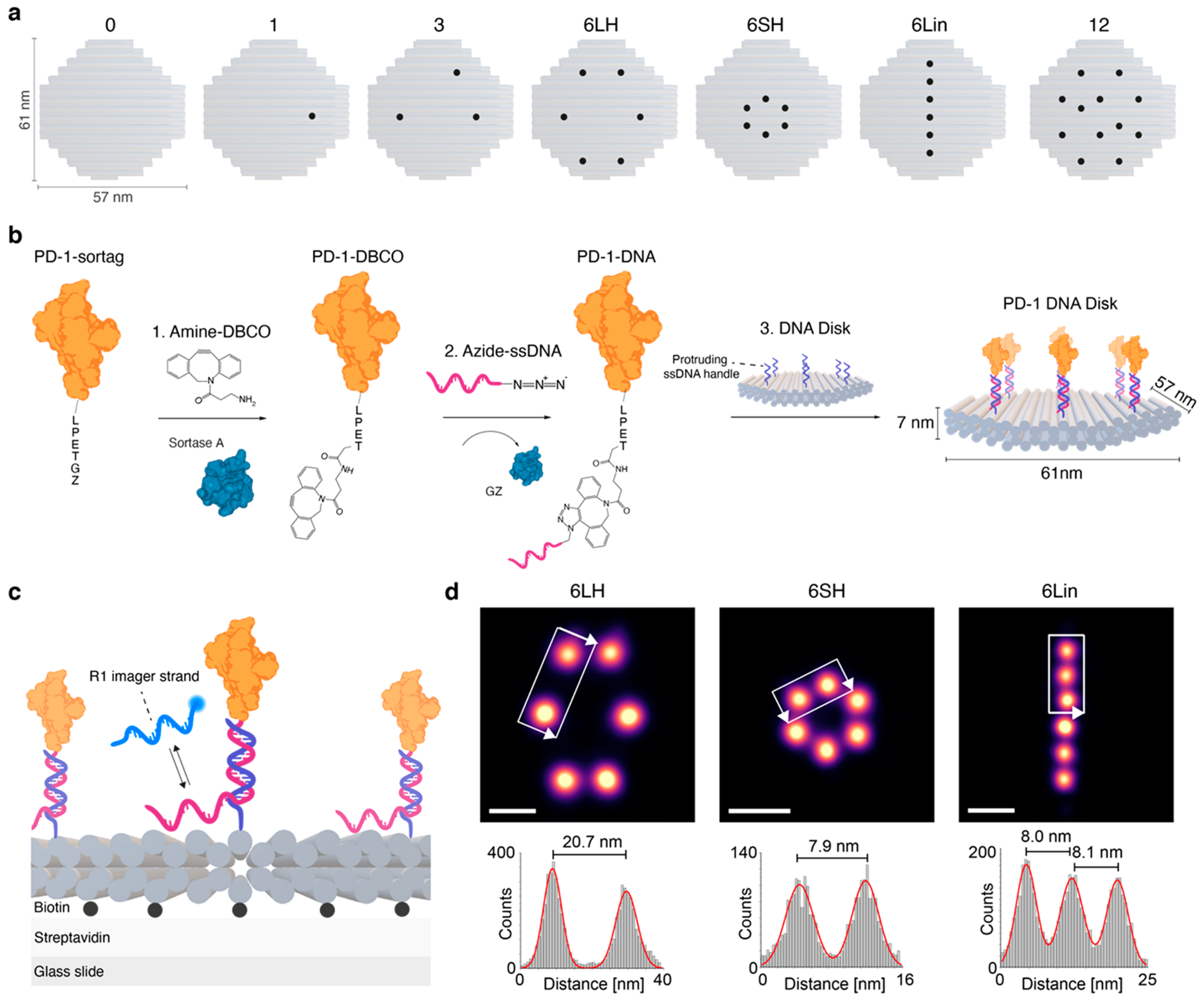

Figure 2. Production of PD-1-DNA conjugates and functionalization on DNA origami disks. (a) Schematic representation of the DNA disk library used to investigate the influence of valency and pattern of PD-1 on the interaction with target ligands. Each black dot represents the position of PD-1 on the DNA disk. (b) Schematic overview of the experimental workflow used to conjugate PD-1 to ssDNA via (1) sortase-mediated reaction and (2) copper-free click chemistry, and (3) hybridize PD-1 to DNA origami disks. Z = poly histidine tag. (c) Schematic representation of the DNA-PAINT experimental setup used for the characterization of 6LH, 6SH, and 6Lin PD-1 DNA disks. PD-1-DNA conjugates were prepared with a ssDNA handle extended with a DNA-PAINT docking sequence (R1). Each PD-1 was visualized by transient hybridization of the imager strand (Cy3B-labeled R1 imager strand) and the docking strand. (d) DNA-PAINT sum images of 6LH, 6SH, and 6Lin PD-1 DNA disks (top). Cross-sectional histogram analysis was performed for the highlighted areas (white boxes) to measure inter-PD-1 distances (bottom). Scale bars: 15 nm.

origami nanoparticles displaying PD-1 proteins into nanoclusters of varying stoichiometries with controlled interligand spacing and geometric patterns. The use of low-affinity recombinant PD-1 proteins instead of high-affinity PD-L1 targeting antibodies allows to understand the effect of cluster valency and pattern spacing in the natural context of this inhibitory pathway. Our findings demonstrate that organizational parameters have a significant impact on the PD-1 binding strength to DCs. Additionally, we find that valency dominates pattern with consequences on the immune blockade efficacy due to balance in binding equilibrium. These findings contribute to the molecular understanding of this significant immune pathway and highlight the importance to carefully consider structural properties in the design of functional materials for immunotherapeutic strategies.

RESULTS AND DISCUSSION

PD-L1 Receptors Organize into Nanoclusters on the DC Surface. DCs typically upregulate PD-L1 expression upon encounter with external stimuli to balance immune activation during antigen-presentation.[38] Up- or downregulation of surface markers implies that the spacing between receptor molecular on the cell-surface decreases or increases, respectively. While intuitively, a nonrandom distribution of surface markers seems expectable, a single-protein mapping of exact positions has thus for not been presented. We started with investigating the change in PD-L1 molecular arrangement on the cell surface of nonactivated 1940 CD8α^+ murine tumor-derived (mutu)DCs (DCs) and DCs activated with CpG and IFNγ for 24 h. To this end, we employed the DNA-PAINT imaging technique as it affords the spatial resolution required to resolve PD-L1 at the single molecule level, thereby providing information on its spatial organization (Figure 1a).[39] DCs adhered to glass slides were first incubated with anti-PD-L1 antibody modified with a short DNA "docking strand" to enable specific detection of single PD-L1 receptors via a complementary "imager strand". The dye-coupled "imager strand" transiently binds to complementary target-bound "docking strand" creating stochastic blinking. The Picasso software package was employed to reconstruct the image where each spot corresponds to a single PD-L1 protein (Figure 1b).[40]

Inspection of the overall PD-L1 density revealed a significant increase in PD-L1 expression after DC stimulation (Figure S1), and we wondered whether the absolute increase in density was associated with a specific receptor organization, or if receptors were organized in a fully random fashion. Nearest neighbor distance (NND) analysis was used to quantify the PD-L1 spatial distribution and generated based on experimental data extracted from at least 12 cells. Experimental NND data were plotted against NND distribution of a complete spatial randomness (CSR) data sets. NND analysis revealed a random PD-L1 organization prior to stimulation as depicted by the overlap of the experimental and CSR distributions (Figure 1c), indicating that PD-L1 molecules do not cluster before stimulation but rather distribute in a uniform fashion on the cell surface. In contrast, nanoscale cluster formation was observed after stimulation as marked by a shift in distribution toward smaller NNDs in comparison to simulated data (Figure 1d). From the experimental NND distribution, a distance of approximately ~25−30 nm between neighboring PD-L1 resulting from clustering was derived. Next, we identified the number of individual PD-L1 molecules per cluster. The order of oligomerization was classified according to the number of constituent molecules including monomers (1 molecule), dimers (2 molecules), trimers (3 molecules), tetramers (4 molecules), and larger nanoclusters (>4 molecules). While the majority of PD-L1 resided in monomers, as would be expected based on the dynamics of the cell membrane and global entropy of the system, we found that PD-L1 can accumulate into nanoclusters of higher oligomer order (Figure 1e). In nonactivated DCs, more than 90% of PD-L1 receptors are detected as monomers. Interestingly, after stimulation we observed significant increases in the percentage of PD-L1 that was arranged into higher oligomer clusters compared to nonactivated DCs, highlighting the dynamic reorganization of PD-L1 on DCs in response to stimulation.

Preparation of Nanocontrolled PD-1 Displays on DNA Origami Disks. We hypothesized that the observed PD-L1 nanoclusters contribute to strong T cell inhibition via the multivalent organization of PD-1. The impact of multivalent binding strongly depends on the monomeric binding strength. Typically, nature employs low-affinity binding partners to ensure reversibility, thus interactions strongly rely on the multivalency effect for temporal stability. Hence, to unravel the importance of spatial organization in functional signaling, it is critical to use the natural (low-affinity) proteins and not a high-affinity antibody. We used the structural parameters found by DNA-PAINT as a template to design PD-1 nanoclusters on DNA origami disk-shaped nanoparticles (DNA disk).[41] This architecture has a diameter of ~60 nm and allows the display of up to 36 molecules with tunable valencies, spacings and patterns, both on the top and bottom face. We took advantage of the flat and rigid shape to present PD-1 proteins on the same plane, which ensures preorientation and equal accessibility for binding. A library of nanocontrolled PD-1 displays with varying valencies (0, 1, 3, 6, and 12) was assembled (Figure 2a). Since patterns are abundant in nature[34,42−45] and are known to affect the selectivity of multivalent interactions,[46] we wondered whether the geometric pattern of PD-1 would be of significant importance. A pattern library of hexavalent DNA disks was assembled presenting PD-1 in large hexagon (LH), small hexagon (SH) and linear (Lin) patterns (Figure 2a). These particles allowed us to simultaneously investigate interligand spacing and geometric pattern effects. For detection purposes, 6× Cy5 molecules were integrated on the opposite side of the DNA disk (Figure S2a). Proper folding and purification of each DNA disk was systematically verified by agarose gel electrophoresis (AGE) (Figure S2b).

For a nanocontrolled presentation of PD-1 on the DNA disk, the protein requires modification with a ssDNA oligonucleotide designed to hybridize to complementary ssDNA "handles" protruding from the DNA disk surface. To ensure a native orientation of PD-1 without compromising its binding activity, we employed a site-specific conjugation method consisting of a sortase (SrtA)-based enzymatic reaction followed by copper-free click-chemistry (Figure 2b). Mouse PD-1 was engineered with a SrtA recognition motif—LPETG (sortag)—upstream to the poly histidine tag at the C-terminus, ensuring the DNA handle to be positioned at the opposite side of the PD-1 epitope-binding region. Successful PD-1 conjugation to a ssDNA handle was confirmed by PAGE analysis (Figure S3).

Relying on the DNA sequence-specific hybridization, PD-1 DNA disks were assembled by annealing PD-1-DNA conjugates with the prefolded DNA disks presenting complementary ssDNA handle extensions in the predetermined positions according to the designs (Figure 2b). Qualitative AGE analysis confirmed the assembly of PD-1 DNA disks, where the sample migration is gradually delayed with increasing PD-1 valency (Figure S4a). For further verification, PD-1 proteins were detected on DNA disks using fluorescently labeled anti-PD-1 antibodies (Figure S4b). As steric hindrance may potentially arise with the attachment of a high number of proteins, we conducted AGE analysis to assess the functionalization efficiency. We therefore folded a panel of DNA disks stepwise increasing their handle presentation from 0 to 12, functionalized or not with PD-1, and incubated with complementary Cy3 antihandles (Figure S5). This qualitative analysis indicated that most handles were occupied by PD-1 as the Cy3 intensity of the PD-1 DNA disks was systematically lower than the signal of the DNA disk construct presenting only one Cy3 antihandle. Similar analysis was performed for each hexavalent construct independently and again indicated that all patterns can display the PD-1 proteins (Figure S6).

We noticed that samples with the same valency of 6 PD-1, but different patterns, systematically exhibited a distinct migration behavior on AGE (Figure S4a). To confirm the exact valency of proteins and allow for a fair comparison between each of the hexavalent patterns in subsequent experiments, we imaged each PD-1 protein on LH, SH and Lin patterns using DNA-PAINT microscopy. PD-1 was equipped with a ssDNA handle extended with a DNA-PAINT docking sequence (R1), allowing for visualizing by transient hybridization with an imager strand (Figures 2c and S7). The DNA-PAINT image reconstruction revealed super-resolved patterns matching the designed arrays (Figure 2d, top). A cross-sectional histogram analysis in the DNA-PAINT

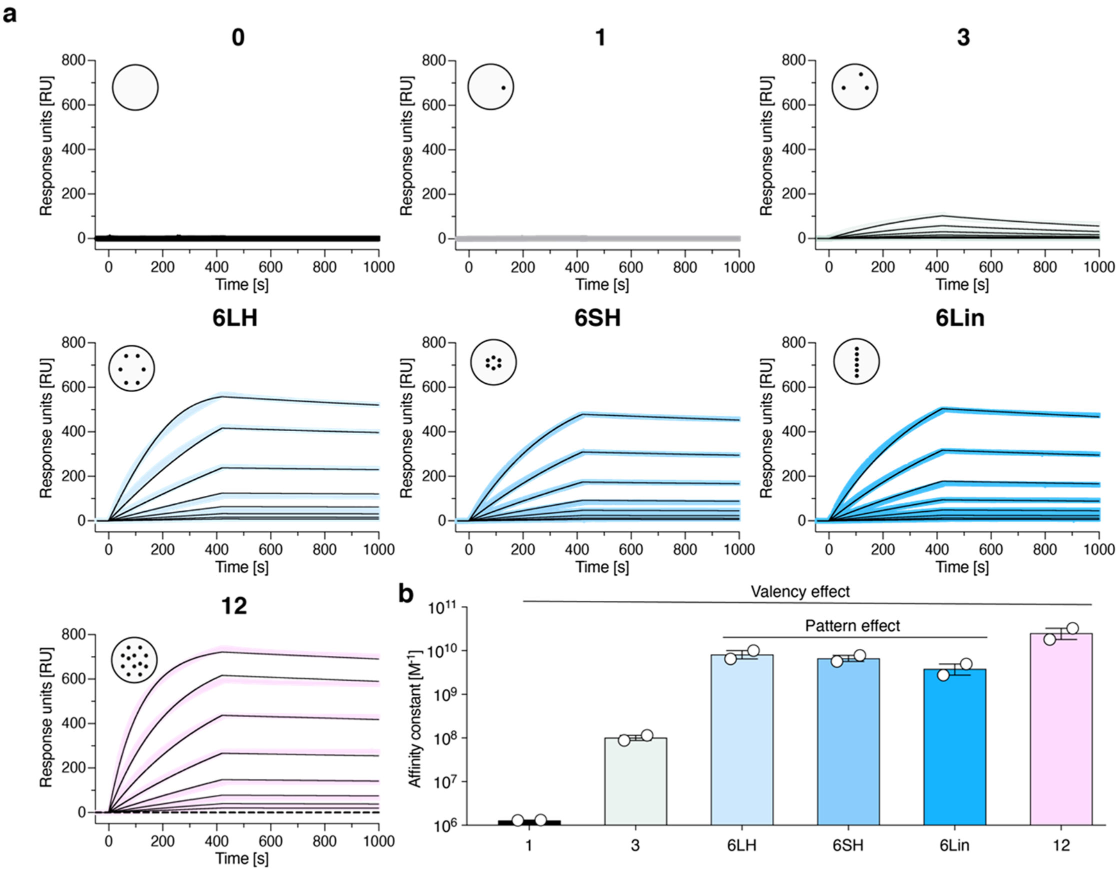

Figure 3. Analysis of PD-1 DNA disk binding behavior on PD-L1 surfaces by SPR. (a) Representative binding curves of DNA disks presenting 0, 1, 3, 6 (in LH, SH, and Lin patterns), or 12 PD-1. Bare DNA disk shows no binding to PD-L1, excluding nonspecific interactions with the ligand. Curves represent increasing particle concentrations (10 nM and 2-fold dilution). (b) Quantification of affinity constants obtained from fitted curves. Error bars indicate SEM (*n* = 2 independent experiments).

Table 1. Binding Parameters of PD-1 DNA Disks with PD-L1 and Comparison to Soluble PD-1, as Measured by SPR

sample	K_D [M]	k_{off} [s^{-1}]	K_D fold increase	relative K_D fold increase[a]
Monomeric PD-1	$7.9 \pm 0.2 \times 10^{-7}$	ND[b]	–	–
3 PD-1 Disk	$1.2 \pm 0.4 \times 10^{-8}$	$1.2 \pm 0.1 \times 10^{-3}$	70	20
6LH PD-1 Disk	$1.4 \pm 0.4 \times 10^{-10}$	$1.4 \pm 0.2 \times 10^{-4}$	5600	900
6SH PD-1 Disk	$1.6 \pm 0.4 \times 10^{-10}$	$1.5 \pm 0.3 \times 10^{-4}$	4900	800
6Lin PD-1 Disk	$2.9 \pm 0.2 \times 10^{-10}$	$1.9 \pm 0.9 \times 10^{-4}$	2700	500
12 PD-1 Disk	$5.6 \pm 1.3 \times 10^{-11}$	$5.1 \pm 1.0 \times 10^{-5}$	14100	1200

[a] Relative to the PD-1 number on the disk. [b] Not determined.

sum image confirmed that the average distances between PD-1 proteins were in accordance with the original distances[41] (Figure 2d, bottom). Using a cluster analysis algorithm,[47] the average number of spots per PD-1 DNA disk was measured and compared to negative controls corresponding to DNA disk mimics with no PD-1 (Figure S8 and Table S1). Evaluation of a minimum of 5000 structures confirmed that all hexavalent PD-1 configurations exhibit comparable presentation of PD-1.

Binding Behavior of PD-1 DNA Disks on PD-L1 Surfaces. Using the fully characterized ensemble of spatially controlled PD-1 decorated DNA disks, we sought to understand whether the presentation of patterns indeed affected the binding behavior with their target PD-L1 using Surface Plasmon Resonance (SPR). First, we determined that the binding affinity, here reported as the equilibrium dissociation constant (K_D), of soluble PD-1 to its ligand PD-L1 is ~1 μM (Figure S9a), which is characteristic of a relatively weak molecular interaction. This value is in good agreement with previous values reported to range from ~1 to ~10 μM.[48−50] We measured the K_D of the PD-1-DNA conjugate at ~3 μM (Figure S9b), indicating that the conjugation procedure did not affect the binding potential of PD-1. Next, we examined how the valency of PD-1 influences the binding profile when presented as multimers on DNA disks compared to the monomeric form (Figure 3a). Nonspecific interactions were excluded as control DNA disk lacking PD-1 showed no binding to the PD-L1 surface. Disks with only one PD-1 were under the detection limit set by the experimental limit in concentration of DNA origami (10 nM). From a PD-1 valency of 3 and upward, we observed a gradual increase in the absolute binding response, indicating a boost in binding strength. A difference of 2 orders of magnitude in dissociation constants, reducing K_D values from ~10^{-8} to ~10^{-10} M, was observed when valency was increased from 3 to 6. This

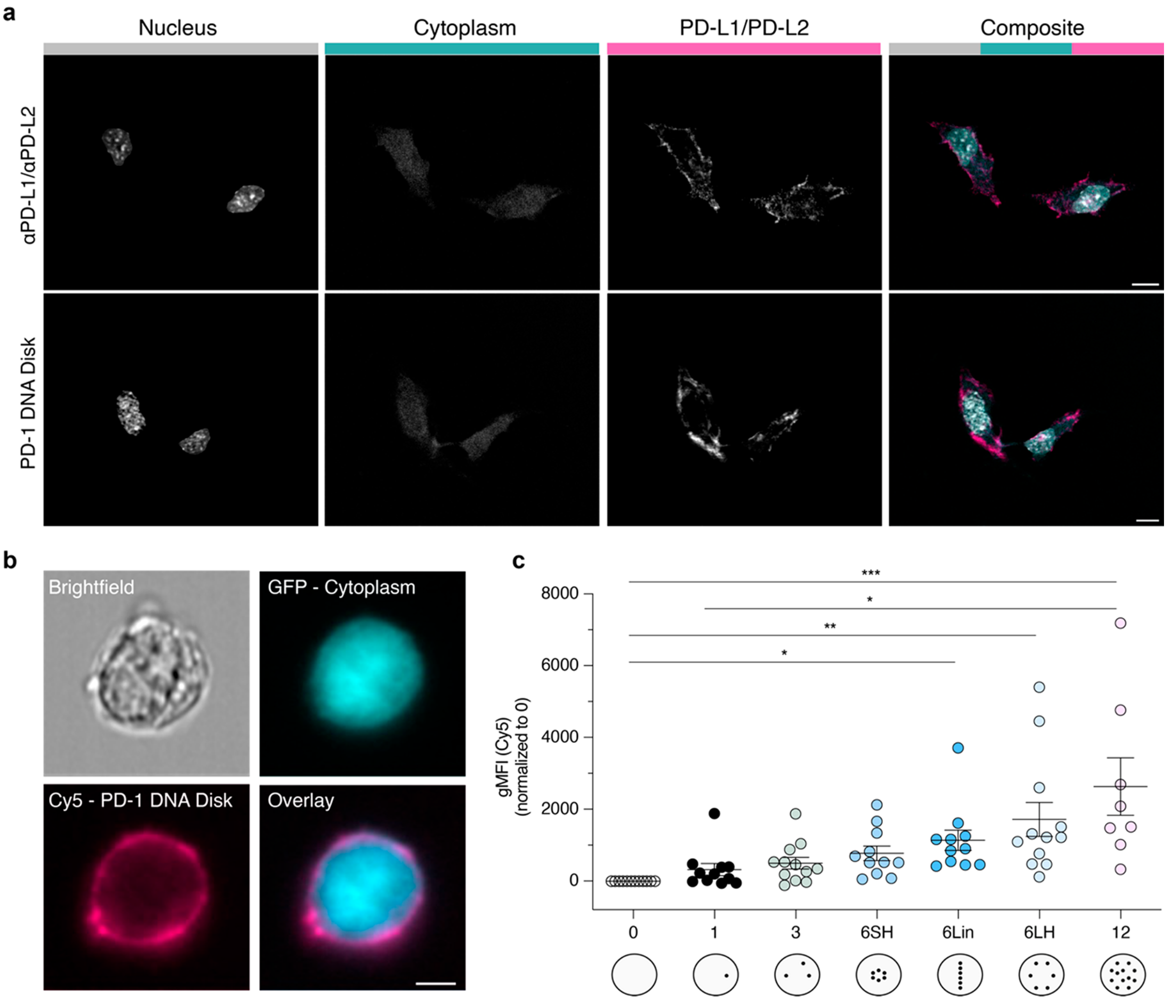

Figure 4. Effect of valency and pattern of PD-1 DNA disks on binding to DCs. (a) Representative confocal microscopy images of the surface staining of DCs using (top) αPD-L1 and αPD-L2 antibodies and (bottom) 12 PD-1 DNA disk. Nucleus stained with DAPI in gray, cytoplasm (GFP reporter in CD11c$^+$) in cyan, and PD-L1/PD-L2 in pink. Scale bars: 10 μm. (b) Representative flow cytometric images of DCs stained with 12 PD-1 DNA disk acquired on Amnis ImageStream system. Cytoplasm (GFP reporter in CD11c$^+$) in cyan and PD-L1/PD-L2 in pink. Scale bar: 5 μm. (c) Binding of PD-1 DNA disks with different valencies and patterns to DCs, presented as the geometric mean fluorescence intensity (gMFI) of Cy5 integrated in the DNA disks. The data were normalized by subtracting the gMFI of the 0 DNA disks for each experiment. Error bars indicate SEM ($n \geq 8$ independent experiments). Raw data of each group (Figure S10f) were compared to each other using a Kruskal–Wallis test, followed by Dunn's post-test (*$p < 0.05$, **$p < 0.01$, ***$p < 0.001$).

suggests that a threshold number of ligands is required for stable multivalent binding, which is in line with our previous observations of multivalent pattern recognition (MPR) in model systems (Figure 3b).[46] This effect was in part due to dissociation rates (k_{off}) slowing down from ~10^{-3} to ~10^{-4} s^{-1} (Table 1). Additional increase to 12 PD-1 enhanced the binding parameters by 1 order of magnitude compared to hexavalent counterparts, yielding a K_{D} of ~10^{-11} M and k_{off} in the ~10^{-5} s^{-1}. Regardless of the spatial configuration, all hexavalent constructs exhibited comparable binding behaviors, yet nuanced differences were detected trending to weaker binding for the most compact PD-1 presentation. Overall, we notice that a multivalent presentation of PD-1 has a significant impact on the dissociation rate compared to the monomeric form, shifting from relatively fast to long-lasting. Furthermore, when comparing K_{D} values between multimeric PD-1 particles and soluble PD-1, the data revealed a notable enhancement in overall binding strength. The K_{D} values decreased over 10,000-fold when the valency was raised to 12, corresponding to an approximate 1000-fold boost in binding avidity per PD-1 protein on the particle (Table 1).

Binding Behavior of PD-1 DNA Disks on the DC Surface. We next wondered how the interaction of PD-1 DNA disks with DCs is influenced by PD-1 valency and geometric patterns, as insights into these parameters could help understand the structural requirements implicated in PD-1-mediated immune regulation. As such, we first verified that PD-1 DNA disks can indeed target the cell surface using the highest PD-1 valency of the library. As DCs typically present low levels of PD-L1 and PD-L2 receptors in nonactivated conditions, DCs were stimulated with CpG and IFNγ to induce their expression. Activation (CD40 marker) and PD-1 ligand (PD-L1 and PD-L2) expression were confirmed by flow cytometry (Figure S10a). Next, the binding of PD-1 DNA disk to DC was characterized by confocal microscopy (Figure 4a). As DCs are professional phagocytes, cells were PFA-fixed prior staining with PD-1 disks to prevent particle internalization. We compared the binding of PD-1 DNA disks to that of specific monoclonal anti-PD-L1 and anti-PD-L2 antibodies (αPD-L1

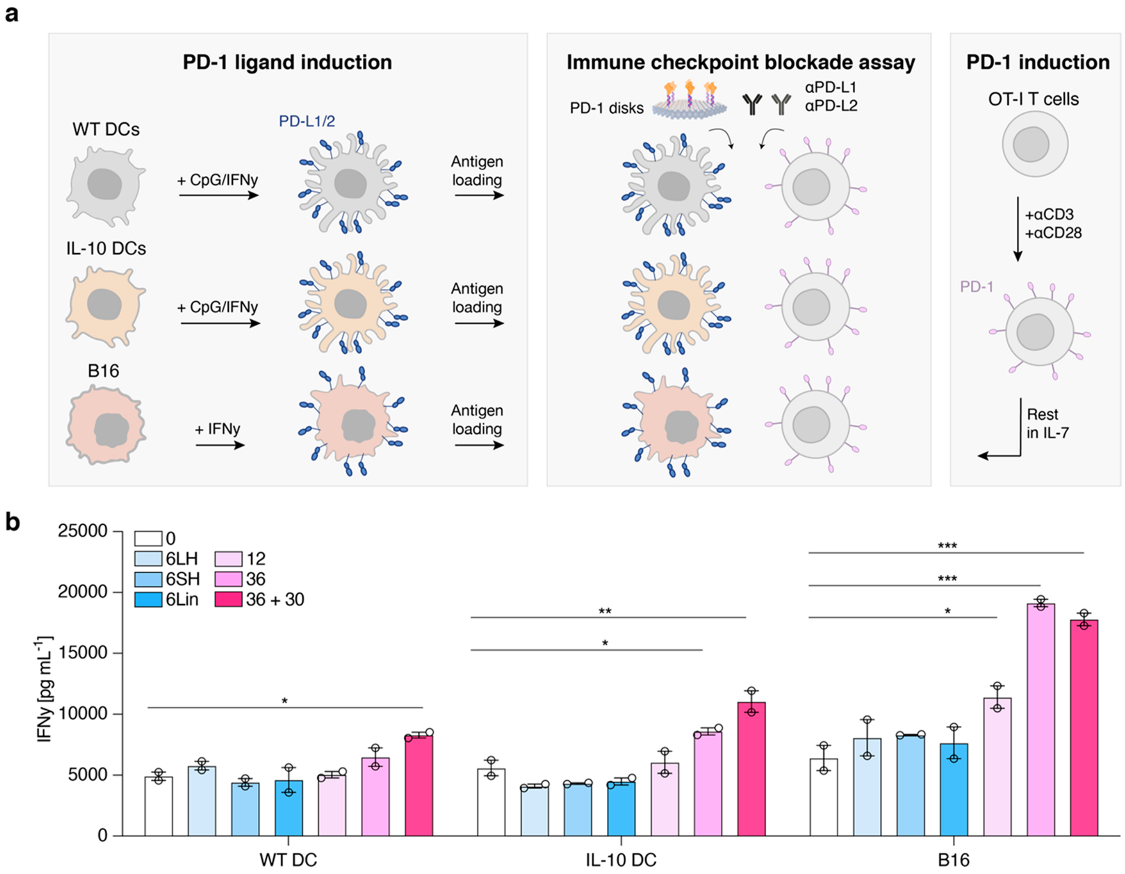

Figure 5. Influence of PD-1 valency and pattern on immune checkpoint blockade. (a) Schematic overview of the experimental setup. Primary CD8α^+ OT-I T cells were stimulated with αCD3/αCD28 antibodies to induce PD-1 expression. After resting in IL-7, T cells were cocultured with stimulated WT DCs, IL-10 DCs or cancer cells (B16) in the presence of PD-1 DNA disks or control blocking αPD-L1/αPD-L2 antibodies. Cytokine production in the supernatants after 24 h was measured as T cell activation readout. (b) Representative IFNγ production after 24 h of blockade with PD-1 DNA disks. Error bars indicate SEM ($n = 2$ replicates in one experiment). Replicates can be found in Figure S15. Statistical analysis was performed independently for each cell type. PD-1 DNA disk groups are compared to 0 DNA disk groups with ordinary one-way ANOVA, followed by Dunnett's test (*$p < 0.05$, **$p < 0.01$, ***$p < 0.001$).

and αPD-L2). Confocal images illustrated a similar staining for both PD-1 disks and the antibodies where most of the signal intensity was localized on the plasma membrane, indicating that DNA origami disks can indeed be applied for surface targeting. To exclude nonspecific interaction with the cell surface from the DNA disk itself, control cells were stained with bare DNA disks, which showed no signal (Figure S10b).

As these data sets indicated that the PD-1 DNA disk is functional within a cellular context, we continued our investigations on the impact of spatial organization of PD-1 using flow cytometry to obtain physiological information on live cells. To ensure long-term stability in culture conditions, PD-1 disks were oligolysine-stabilized.[51] Interaction with the plasma membrane of activated DCs was confirmed by imaging flow cytometry, where we observed the absence of Cy5 signal within the cytoplasmic compartment which was defined by the GFP reporter in the DCs (Figures 4b and S10c). We then used a similar staining procedure to investigate the influence of PD-1 valency and pattern on binding to DCs, analyzed at the single cell level by standard flow cytometry. The results demonstrate a profound valency effect as we observed a higher fluorescence intensity with increasing numbers of PD-1 per disk (Figure 4c). The data again confirmed that a minimum number of six ligands is required to provide a strong and stable binding to DCs. Interestingly, valency alone does not fully determine the binding profile of a multivalent PD-1 presentation; the geometric PD-1 arrangement had a significant impact on the binding strength, thereby guiding multivalent pattern-specific interactions (Figure 4c). When PD-1 nanoclusters were presented into a larger circular assembly (6LH), binding was favored in contrast to a more compact arrangement (6SH), or when organized into a linear pattern (6Lin), which showed less pronounced differences in binding. This emphasizes the importance of interligand spacing and geometric pattern as crucial determinants of binding efficiency.

Finally, we studied how these results compare to ligand targeting with classical specific antibodies. Unlabeled αPD-L1 antibodies were placed on DNA disks in a 6LH configuration to respect a uniform valency and fluorescence signature among all samples. We observed significant binding differences relative to empty DNA disks (Figure S10d), with absolute signals similar to 6LH PD-1 DNA disk but lower than 12 PD-1 DNA disk. These observations suggest that multivalent ligand presentation can boost the binding avidity of a weak binder (the recombinant PD-1 protein) to receptors on the cell surface and that multimerization of a stronger binder, such as antibodies, does not further enhance the binding strength. To further demonstrate the specificity of these interactions, DCs were blocked with soluble αPD-L1 and αPD-L2 prior to staining. For both PD-1 DNA disks and αPD-L1 DNA disks, binding was abrogated when target receptors were blocked from binding (Figure S10e,f), indicating that the observed interactions were predominantly ligand-specific. Altogether these findings provide evidence that both nanoclustering via multivalency and spatial arrangement, such as cluster profile and spatial geometry, of immune regulator PD-1 are important factors in modulating the PD-1 interaction strength with target cells.

A High Valency of PD-1 on DNA Disks Restores T Cell Function. To understand the biological implication of the spatial organization of immune regulator PD-1 on T cell function, we turned to coculture experiments to test the blocking efficiency of PD-1 DNA disks (Figure 5a). In their role as antigen-presenting cells (APCs), DCs modulate their phenotype to a tolerogenic or immunogenic state in order to guide T cell function accordingly.[52,53] In the context of the PD-1 pathway, tolerogenic DCs play a role in T cell suppression to maintain homeostasis, while immunogenic DCs put a brake on T cell effector activity during infection to avoid autoimmunity.[4,38,54] We therefore studied whether the blocking efficacy of PD-1 DNA disks varied depending on the DC phenotype. We included WT DCs and IL-10-secreting DCs (IL-10 DCs) as immunogenic and tolerogenic DC models, respectively (Figure 5a). The tolerogenic features of IL-10 DCs were previously characterized by significant downregulation of stimulatory surface markers such as MHC-II, CD40, CD80, and CD86 compared to WT DCs upon stimulation.[55] Additionally, we used the B16 melanoma line (B16) as a tumor cell model that expresses PD-L1 to investigate how the blocking efficacy compares to DCs, as tumor cells are known to inhibit immune activation (Figure 5a). All target cells were stimulated to induce PD-1 ligand expression (Figure S11) and peptide-pulsed (SIITFEKL) prior to coculture. Separately, primary CD8α^+ T cells were isolated and purified from OT-I transgenic mouse (Figure S12a), whose T cells express transgenic T cell receptors that can recognize the SIITFEKL epitope. To induce their PD-1 expression, freshly isolated T cells were stimulated for 24 h with αCD3 and αCD28 antibodies, and then rested before coculturing with APCs (Figure S12b). The blockade efficacy was characterized via the production of inflammatory cytokines (IFNγ, TNFα, and IL-2) by T cells after 24 h of coculture.

We observed that when SIITFEKL-presenting APCs interacted with T cells in the presence of blocking αPD-L1/αPD-L2 antibodies, T cell produced significantly higher levels of IFNγ compared to when no blocking agent was present (Figure S13a). This confirms that blocking antibodies can indeed restore T cell activity via PD-1 blockade in this coculture setup. TNFα and IL-2 analysis revealed similar, yet more moderate, trends (Figure S13b,c). The readouts of this complex biological pathway results from a delicate interplay of interactions between material:cell, cell:cell, cell:time, and material:time, with time playing a role in the kinetics of signaling, stability of the interaction, stability of the material, and viability of cells. Hence, fluctuations in blocking efficacy are to be expected and for our PD-1 disk performance, we first had to establish a suitable working valency that was compatible with the timing of the assay. Upon initial analysis of the blockade performance of our PD-1 DNA disk library, we found that DNA disks with low PD-1 valency (6 and lower) were not sufficiently potent. We thus decided to test the performance of our blocking reagents in valencies of 6 (in three patterns), 12, as well as at higher valencies, including 36 and a dual-functionalized disk with 36 + 30 PD-1 molecules utilizing all accessible conjugation sites (Figure S14), to maximize the longevity of communication to the APCs. Interestingly, when we assessed the influence of PD-1 spatial organization on the T cell activity, we found that valency determines the blockade efficacy (Figures 5b and S15). Indeed, high valencies were required to generate significant PD-1-mediated blockade. As the lower valency-induced responses were below background levels, it unfortunately prevented us to distinguish any pattern effect.

A strong correlation was observed between APC phenotype and therapeutic effects of PD-1 DNA disk blockade with more pronounced differences for cancerous phenotypes versus tolerogenic and immunogenic DC phenotypes. This finding indeed suggests that specific cell types are more responsive to PD-1, potentially depending on the number of binding events of the PD-1 disks. Specifically, cancer cells were more susceptible to blockade at lower PD-1 valency with 12 PD-1 in contrast to DC types for which at least 36 PD-1 were required. Curious to these differences, we verified CD80 expression on the various APCs, as this costimulatory receptor is known to sequester PD-L1,[56] thereby potentially decreasing the binding probability of PD-1 to PD-L1, which could have implications in the blocking process. Indeed, CD80 expression decreases toward immunogenic > tolerogenic phenotypes and is almost absent in cancer cells (Figure S16). With lower amounts of CD80 available, more PD-L1 is accessible, hence the lower valency PD-1 disks are more effective. However, interactions in checkpoint biology are multifactorial and more complex than the singular CD80-PD-L1 example discussed here, as the interplay with other factors is crucial in determining how regulatory pathways intersect.[57] Overall, our results suggest that valency, i.e., the number of interacting PD-1, is the determinant factor for efficient PD-1 blockade, as simultaneous binding of sufficient PD-1 molecules may be required to form a stable and long-lasting contact with APCs and consequently influences T cell signaling.

CONCLUSION

In this study, we set out to explore the functional impact of spatial organization of immune checkpoint receptor PD-1 by manipulating structural parameters such as nanoclustering, oligomer valency, but also pattern on DNA origami nanoscaffolds. We hypothesized that preconfigured PD-1 structures that favor T cell inhibition may also be present on the DC surface in the form of matching PD-L1 nanoclusters. A super-resolved analysis of the PD-L1 distribution on DCs revealed that upon activation, PD-L1 reorganizes into nanoscale domains that can accommodate oligomers of higher orders. These insights in spatial distribution were used to construct nanocontrolled PD-1 platforms using a rigid, flat DNA origami structure with complete control over valency and ligand positioning while ensuring full binding potential of PD-1 using a site-specific conjugation method.

A strong valency effect was observed both in surface targeting as well as in functional communication. We observed that a minimum number of ligands of six was needed to provide strong and stable binding to DCs, suggesting that PD-1 nanoclustering via multivalency is an important factor in modulating the binding strength for surface targeting. In a functional setting, we observed that valency was the dominating factor for efficient PD-1-mediated blockade on T cells due to a balance in binding equilibrium and longevity of the functional interaction.

In addition to clustering, we found that the spatial proximity of PD-1 molecules within the nanocluster modulates their adhesion to the cell surface. While a more compact configuration (6SH) displayed minimal binding, larger spaced assemblies (6LH) exhibited stronger interactions with target cells. Interestingly, the inter-PD-1 geometric mean distance in the strongest binding 6LH pattern measured at ∼25 nm, matches with the inter-PD-L1 distances initially derived by DNA-PAINT microscopy in contrast to 6SH with an average PD-1 spacing of 10 nm.[46] Additionally, we observed that a circular PD-1 pattern (6LH) exhibited stronger binding than the linear counterpart (6Lin). Although these particles display the same valency, the distinction in distances and geometric patterns contribute to the differences in cell binding. This highlights the importance of tailoring the design parameters of multivalent materials based on the natural molecular organization present on cells to achieve selective recognition. In cellular biology, selectivity can be described as the ability of multivalent ligands to selectively bind to specific receptors on cells, based on the precise structural complementarity between receptors and ligands.[58−60] To achieve optimal binding, the arrangement of ligands on the donor cell typically orchestrates the organization of receptors on the recipient cell. This concept has important implications for various biological processes, including immune response and cell signaling, where immune cells can distinguish between healthy and abnormal cells. Therefore, we believe that in the case of PD-1/PD-L1 axis, developing functional inhibitors that can selectively block the interaction between PD-1 and PD-L1 without affecting other immune pathways would be highly beneficial for active nanomaterials in cancer therapy.

MATERIALS AND METHODS

Materials. Thermo Fisher Scientific (Waltham, MA, USA) provided Iscove's Modified Dulbecco's Medium (IMDM) Glutamax supplement (Gibco, 31980030), Penicillin−Streptomycin (Gibco, 15140122), HEPES for cell culture (Gibco, 15630−056), sodium bicarbonate for cell culture (Gibco, 25080094), EDTA for cell culture (Alfa Aesar, J60292), β-mercaptoethanol for cell culture (Gibco, 31350−010), 0.45-μm filters (Corning, 09−761−53), HEPES solution (J16924.AP), NaCl solution (S5150), β-d-thiogalactoside (IPTG) (34060), Salmon Sperm DNA (15632011), Endotoxin Removal Spin Columns (88276), Endotoxin quantification kit (A39552S), 7K MWCO Zeba Spin Desalting Columns (89883), HisPur Ni-NTA resin (88221), Pluronic F-127 (Invitrogen, P6867), Tris-Glycine 4−20% Novex gel Mini (Invitrogen, XP04205BOX), Micro BCA Protein Assay kit (23235), TBE solution (Acros Organics, ACR32733−0010), SYBR safe (Invitrogen, S33102), 1× PBS (Gibco, 20012019), NeutrAvidin (31000), 4% Paraformaldehyde (Alfa Aesar, J61899), Normal Rat Serum (NRS) (Invitrogen, 10710C), Alexa Fluor 647 antirat antibody (Invitrogen, S21374), ProLong Glass mounting media (Invitrogen, P36982), eBioscience Fixable Viability Dye eFluor 780 (Invitrogen, 65−0865−14), PE-Cy5 antimouse CD80 (16−10A1, 15080182), SYPRO Ruby Protein Gel Stain (Invitrogen, 1703126), Dulbecco's Modified Eagle Medium (DMEM), high glucose, pyruvate (Gibco, 41966029), trypsin-EDTA solution (Gibco, 25200056), Roswell Park Memorial Institute (RPMI) 1640 Medium, GlutaMAX Supplement (Gibco, 61870010), eFluor 450 antimouse CD25 antibody (PC61.5, 48−0251−82), high-binding 96-well plate (Corning, 10440862), Mouse Uncoated ELISA Kit (Invitrogen, 88−7314−88), TNF alpha Mouse Uncoated ELISA Kit (Invitrogen, 88−7324−88) and IL-2 Mouse Uncoated ELISA Kit (Invitrogen, 88−7024−88). PAN-Biotech GmbH (Aidenbach, Germany) provided FBS Gold for DCs (P30−3033). Twist Biosciences (San Francisco, CA, USA) provided PD-1 plasmid (pTwist CMV BetaGlobin WPRE Neo) and SrtA plasmid (pET29b+). Merck KGaA (Darmstadt, Germany) provided Tween-20 (Sigma-Aldrich, P9416−50 ML), *E. coli* BL21(DE3) (Novagen, 70235), glycerol (Sigma-Aldrich, G9012), amine-dibenzocyclooctyne (amine-DBCO) (Sigma-Aldrich, 761540), CaCl$_2$ solution (Sigma-Aldrich, 21115), 30k MWCO Amicon centrifugal filters (Millipore, UFC503096), Tris solution (Millipore, 648314), MgCl$_2$ solution (Sigma-Aldrich, M1028), agarose powder (Sigma-Aldrich, A9539), 100k MWCO Amicon centrifugal filters (Millipore, UFC510096), Glass slides (10756991), 3,4-dihydroxybenzoic acid (PCA) (Sigma-Aldrich, 37580−25G-F), NaOH solution (1091361000), protocatechuate 3,4-dioxygenase pseudomonas (PCD) (Sigma-Aldrich, P8279), ((±)-6-hydroxy-2,5,7,8-tetra-methylchromane-2-carboxylic acid (Trolox) (Sigma-Aldrich, 238813), methanol (Sigma-Aldrich, 32213), BSA (A3294), NHS-Dibenzocyclooctyne (NHS-DBCO) (Sigma-Aldrich, 761524) and 50k MWCO Amicon centrifugal filters (Millipore, UFC505024). Protein Ark Ltd. (Rotherham, UK) provided nickel-bound chelating agarose resin (Fastback-Ni-Adv-25). Cytiva Europe GmbH (Freiburg im Breisgau, Gemany) provided Superdex 200 Increase 10/300 GL (28990944), HisTrap HP column (17524802), HiLoad 16/600 Superdex 200 pg (28989335), Series S Sensor Chip CM3 (BR100536) and EDC/NHS coupling kit (BR100050). LubioScience GmbH (Zürich, Switzerland) provided QuickBlue Protein Stain (LU001000). Integrated DNA Technologies (IDT) (Coralville, IA, USA) provided DNA oligonucleotides used for DNA origami preparation and CpG ODN 1826 for cell stimulation. Tilibit nanosystems GmbH (Munich, Germany) provided p7560 DNA scaffold for DNA origami preparation. Promega Corporation (Madison, WI, USA) provided poly-ethelene-glycol (PEG) 8000 power (V3011). Biolegend (San Diego, CA, USA) provided Recombinant Mouse IFNγ (575306), FITC antimouse PD-1 antibody (29F.1A12, 135213), purified antimouse CD16/32 antibody (93, 101302), purified antimouse PD-L1 antibody (10F.9G2, 124302), purified antimouse PD-L2 antibody (TY25, 107202), PE-Cy7 antimouse PD-L1 antibody (10F.9G2, 124314), BV421 antimouse PD-L2 antibody (TY25, 107219), PE antimouse CD40 antibody (3/23, 124610), PE-Cy5.5 antimouse CD8α antibody (53−6.7, 100720), Ultra-LEAF antimouse CD3 antibody (17A2, 100238), Ultra-LEAF antimouse CD28 antibody (37.51, 102116), Recombinant Mouse IL-7 (577802), APC antimouse CD8α antibody (53−6.7, 100712) and PE antimouse CD3 antibody (145−2C11, 100308). Avantor (Radnor, PA, USA) provided poly-ethelene-glycol) and 40-μm cell strainer (VWR, 431750). Marienfeld Superior (Lauda-Königshofen, Germany) provided the coverslips (0107242). Laysan Bio Inc. (Arab, AL, USA) provided PEG for DNA-PAINT (MPEG-SVA-5000−1g) and biotin-PEG for DNA-PAINT (BIO-PEG-SVA-5K). Carl Roth GmbH (Karlsruhe, Germany) provided KCl powder (6781.1) and Triton X-100 (6683.1). Cytodiagnostics Inc. (Burlington, ON, Canada) provided gold nanoparticles (G-90−100). Bio-Techne Corporation (Minneapolis, MN, USA) provided recombinant mouse PD-L1-Fc protein (R&D systems, 1019-B7−100). Alamanda polymers (Huntsville, AL, USA) provided K$_{10}$-PEG$_{1K}$ (mPEG$_{1K}$-*b*-PLKC$_{10}$). Ibidi GmbH (Gräfelfing, Germany) provided 12-well Ibidi plate (81201). Abcam (Cambridge, UK) provided DAPI staining solution (ab228549). STEMCELL Technologies (Vancouver, BC, Canada) provided EasySep Mouse CD8$^+$ T Cell Isolation Kit (19853). BD Biosciences (Franklin Lakes, NJ, USA) provided stain buffer (554657) and FITC antimouse CD3 antibody (145−2C11, 553061). Capricorn Scientific (Ebsdorf, Germany) provided FBS Advanced for B16 and T cells (heat-inactivated, FBS-11A). AnaSpec (Fremont, CA, USA) provided SIITFEKL (AS-64403). InvivoGen (San Diego, CA, USA) provided Primocin (ant-pm-2).

DNA-PAINT Imaging of PD-L1 on DCs. *Buffers.* The following buffers were used for sample preparation and imaging: Buffer A: 1× PBS, 500 mM NaCl; Buffer B: 1× PBS, 1 mM EDTA, 0.01% Tween-20; Buffer C: 1× PBS, 1 mM EDTA, 0.02% Tween-20, 0.05% NaN$_3$, 2% BSA, 0.05 mg mL^{-1} sheared salmon sperm DNA.

Enzymatic Antibody-DNA Conjugation. Prior functionalization unconjugated anti-PD-L1 antibody were concentrated to 1 mg mL^{-1}

in TBS + 0.05% Tween-20 by using 50k MWCO Amicon Ultra centrifugal filters. PNGase (0.6 U), mTG (1.2 U) and an 80-fold molar excess of bifunctional azide-PEG3-amine linker were added to the antibody and reacted for 16 h at 37 °C, 300 rpm. Enzymes and excessive linker were removed by buffer exchange to PBS using 30k MWCO Amicon Ultra centrifugal filters. Azido-modified antibodies were reacted with 10-fold molar excess of DBCO-functionalized DNA (7xR4 − ACACACACACACACACACA)[61] overnight at 25 °C, 300 rpm. Unreacted DNA and unconjugated antibody were removed by anion exchange chromatography using an ÄKTA pure system equipped with a Resource Q 1 mL column and antibody concentration was adjusted to 5 μM. DNA-conjugated antibodies were stored at 4 °C until further use.

Sample Preparation for PD-L1 DNA-PAINT Imaging. 2.5×10^4 cells/well were seeded and allowed to adhere overnight. Cells were stimulated using 200 nM CpG and 100 U mL^{-1} IFNγ for 24 h at 37 °C. Unstimulated cells served as a reference. The 4% PFA solution was preheated to 37 °C before addition to the cells. Cells were fixed in 4% PFA for 15 min and washed with PBS. Cells were permeabilized in 0.125% TritonX-100 dissolved in PBS for 1 min, washed with PBS followed by surface passivation with Buffer C for 60 min at 24 °C. DNA-conjugated anti-PD-L1 antibody were dissolved in Buffer C and added at a final concentration of 50 nM overnight at 4 °C. Unbound antibodies were removed by washing with Buffer B, followed by washing once with Buffer A for 5 min. Postfixation was performed with 2% PFA in PBS for 5 min. Prior to the addition of gold fiducials, samples were washed with PBS. Subsequently, 250 μL of 90 nm standard gold nanoparticles, diluted 1:3 in PBS, were added and incubated for 5 min before washing with PBS. Cy3-imager DNA (R4 − GTGTGT)[61] was diluted as shown in Table S2.

Microscope Setup. Fluorescence imaging was carried out on an inverted microscope (Nikon Instruments, Eclipse Ti2) with the Perfect Focus System, applying an objective-type TIRF configuration equipped with an oil-immersion objective (Nikon Instruments, Apo SR TIRF ×100, NA 1.49, Oil). A 560 nm laser (MPB Communications, 1 W) was used for excitation. The laser beam was passed through a cleanup filter (Chroma Technology, ZET561/10) and coupled into the microscope objective using a beam splitter (Chroma Technology, ZT561rdc). Fluorescence was spectrally filtered with an emission filter (Chroma Technology, ET600/50m and ET575lp) and imaged on an sCMOS camera (Andor, Zyla 4.2 Plus) without further magnification, resulting in an effective pixel size of 130 nm (after 2 × 2 binning). The readout rate was set to 540 MHz. Images were acquired by choosing a region of interest with a size of 512 × 512 pixels. Imaging conditions for the respective experiments are shown in Table S2.

Image Analysis. Raw fluorescence data were subjected to super-resolution reconstruction using the Picasso software package[40] (latest version available at https://github.com/jungmannlab/picasso). Drift correction was performed with a redundant cross-correlation and gold particles as fiducials for cellular experiments. DNA-PAINT data were analyzed using the Picasso clustering algorithm (latest version available at https://github.com/jungmannlab/picasso). Circular clusters of localizations centered around local maxima were identified and grouped. Subsequently, the centers of the localization groups were calculated as weighted mean by employing the squared inverse localization precisions as weights.

Data Analysis: PD-L1 Organization. In order to quantify the spatial interactions of PD-L1, Nearest-Neighbor Distance (NND) based analysis was performed for data sets of unstimulated and stimulated cells. First, the NND of each PD-L1 molecule was computed. Then, the experimental histogram of NND was compared to simulations at complete spatial randomness (CSR). PD-L1 molecules were classified as oligomers by using an interaction distance cutoff of 30 nm.

Protein Production and Purification. *Mouse PD-1.* The gene encoding the extracellular domain of the mouse PD-1 protein (residues 25−167; UniProt: Q02242; unpaired cysteine at position 83 was replaced with serine to prevent protein dimerization) was designed with a C-terminal sortase recognition motif (LPETG) followed by a 10x-His tag. The engineered PD-1 gene was cloned into pTwist CMV BetaGlobin WPRE Neo. The protein was expressed in HEK293 cells and supernatant was collected after 7-day post transfection. The supernatant was filtered (0.45 μm) and purified by affinity resin (nickel-bound chelating agarose resin) and subsequent size exclusion chromatography (SEC) using a Superdex 200 Increase 10/300 GL column on ÄKTA systems. The purity of PD-1 protein was evaluated by SDS-PAGE stained with Coomassie blue (Figure S17). The protein was stored at −80 °C until further use.

Sortase A5. The sequence encoding for sortase A5 pentamutent (SrtA) enzyme was obtained from Addgene (Plasmid #75144). SrtA gene was cloned with a C-terminal 6x-His tag into pET29b(+) vector by gene synthesis. Briefly, SrtA was expressed in *E. coli* BL21(DE3) upon IPTG induction (0.5 mM, OD_{600} −0.6) for ∼16 h at 30 °C. Cells were then harvested and lysed by sonication. Protein was purified from lysate supernatant by affinity chromatography on HisTrap HP column and subsequent SEC using a HiLoad 16/600 Superdex 200 pg column. SrtA purity was assessed by SDS-PAGE stained with Coomassie blue (Figure S18). Endotoxins were removed using Endotoxin Removal Spin Columns and levels were measured with an endotoxin quantification kit following manufacture's information. Endotoxin levels were compliant with FDA guidelines. The protein was stored at −80 °C until further use.

PD-1-DNA Site-Specific Conjugation and Purification. PD-1 protein was modified with a DBCO reactive group via sortase-mediated ligation, and was subsequently reacted to an azide-modified ssDNA strand (azide-ssDNA) by copper-free click chemistry as previously described.[62] Briefly, 10 μM PD-1, 10 μM SrtA, and 2 mM amine-DBCO were mixed in sortase buffer (20 mM HEPES pH 7.4, 150 mM NaCl, 10 mM CaCl_2) and incubated for ∼16 h at 4 °C while rotating. The reaction mixture was buffer exchanged into 20 mM HEPES, 150 mM NaCl using 7K MWCO Zeba Spin Desalting columns to stop the reaction and remove excess of amine-DBCO substrate. PD-1-DBCO conjugate was purified by affinity resin (HisPur Ni-NTA). PD-1-DBCO conjugate was then mixed with a 2.5- to 5-fold molar excess of azide-ssDNA and incubated for ∼16 h at 4 °C while rotating. Excess azide-ssDNA was removed using 30k MWCO Amicon Ultra centrifugal filter device precoated with 5% Pluronic F-127 (w/v). The sample was washed repeatedly until no azide-ssDNA was detected in the flowthrough as measured by UV absorption at 260 nm. The concentration of the PD-1-DNA conjugates was determined using a Micro BCA assay kit according to manufacturer's instructions. To confirm the presence of the DNA handle on PD-1, the conjugate was incubated with a 2-fold molar excess of complementary Cy3-labeled oligonucleotide (Cy3-cDNA) for 1 h at 30 °C. Conjugation, purity and hybridization of the Cy3-oligonucleotide were evaluated by native and SDS-PAGE (Figure S3). Gels were imaged using a Chemidoc MP imaging system (Bio-Rad) with fluorescence transillumination and then stained with Coomassie blue. The conjugates were stored at 4 °C until further use.

DNA Disk Preparation and Purification. DNA origami disks were prepared as previously described.[41] Briefly, the folding reaction mixture was prepared by mixing 10 nM of p7560 ssDNA scaffold with 10-fold molar excess of each DNA staple strand in folding buffer (5 mM Tris pH 8, 1 mM EDTA, 5 mM NaCl and 18 mM MgCl_2). Cy5-modified DNA strands were included in the staple pool at a 5-fold molar excess. The folding reaction mixture was subjected to a thermal annealing ramp according to the following program: 5 min at 80 °C, followed by 1 h interval for each temperature starting at 60 °C down to 20 °C, decreasing by 1 °C every step. Folded DNA disks were purified from excess staple strands with two rounds of PEG precipitation protocol.[29] For that, folded structures were mixed 1:1 (v/v) with precipitation buffer consisting of 15% PEG8000 (w/v) diluted in 5 mM Tris pH 8, 1 mM EDTA, 500 mM NaCl and 18 mM MgCl_2. After the second PEG precipitation, folded DNA pellets were resuspended in 10 mM HEPES pH 7.4, 150 mM NaCl, 18 mM MgCl_2. To validate structure folding, samples were analyzed by agarose gel electrophoresis (AGE). DNA disk samples were loaded on a 1% agarose gel (0.5× TBE, 8 mM MgCl_2, 1× SYBR Safe) and gel was run at 70 V for 90 min in an ice−water container. Gels were imaged using fluorescence and UV transillumination. The images were processed using Image Lab software. DNA origami disk concentration was measured by UV absorbance at 260 nm on a spectrophotometer (Q9000, Quawell). Stock samples were stored at 4 °C for short-term use or at −80 °C otherwise.

DNA sequences are available in the Supporting Information (Tables S3−S9).

PD-1 DNA Disk Preparation and Characterization. DNA disks were incubated with 7.5- to 10-fold molar excess of PD-1-DNA conjugate per protruding handle on DNA disk surface for 1 h at 28 °C followed by 14 h at 22 °C. Excess PD-1-DNA conjugate was removed by buffer exchange using 100k MWCO Amicon Ultra centrifugal filter device precoated with 5% Pluronic F-127 (w/v). The PD-1 disk samples were washed 6× with 10 mM HEPES pH 7.4, 150 mM NaCl, 18 mM $MgCl_2$ and, the concentration was determined by UV absorbance at 260 nm. Validation of PD-1 annealing to DNA disks was performed by (1) qualitative analysis of band size shift by AGE (2% agarose gels, 0.5× TBE, 8 mM $MgCl_2$, 1× SYBR safe). Additionally, (2) PD-1-specific detection was done by mixing 10 nM mPD-1 DNA disks with 40 nM FITC antimouse PD-1 antibody. After incubation for 15 min at RT, the samples were analyzed by AGE (1% agarose, 0.5× TBE, 8 mM $MgCl_2$). (3) The functionalization efficiency was assessed by qualitative AGE analysis. For that, DNA disks presenting or not PD-1 were incubated with Cy3 handles, complementary to the handles protruding from the DNA disk. The Cy3 fluorescence in PD-1-functionalized DNA disks samples were compared to the signal from Cy3 DNA disks lacking PD-1 to estimate the functionalization efficiency. All gels were run at 70 V for 3 h in ice−water containers.

DNA-PAINT Characterization of 6LIN, 6SH, and 6Lin PD-1 DNA Disk Constructs. *Sample Preparation.* Preparation of PD-1 DNA disk samples for DNA-PAINT imaging was performed as described above with the following modifications. For imaging purposes, samples were prepared using PD-1 protein modified with ssDNA handles extended with a DNA-PAINT docking strand at their 3′ end. A “TT” spacer was added in between this docking sequence and the sequence that is complementary to the DNA disk handles. A “TT” spacer was also included in the DNA disk handles, in between the part sticking out and the part within the structure. Biotin handles (7×) were integrated on the bottom plane of the DNA disk to allow anchoring of the DNA disks onto BSA-biotin-neutravidin functionalized imaging glass slide. DNA sequences can be found in the Supporting Information (Tables S10 and S11).

Buffers. The following buffers were used in DNA-PAINT imaging: Buffer D: 1 mM EDTA, 500 mM NaCl in PBS pH 7.4; 40× PCA: 154 mg PCA was dissolved in 10 mL MQ and adjusted to pH 9.0 using NaOH; 100× PCD: 9.3 mg PCD was dissolved in 13.3 mL of 100 mM Tris-HCl pH 8, 50 mM KCl, 1 mM EDTA and 50% glycerol; 100× Trolox: 100 mg Trolox was dissolved in 3.2 mL MQ complemented with 430 μL 100% methanol and 345 μL 1M NaOH; Imaging buffer: Buffer D supplemented with 1× PCA, 1× PCD and 1× Trolox.

Microscopy Slide Preparation. Surface passivation of glass slides and coverslips with PEG was performed as described previously.[63] Until further use, slides and coverslips were stored in nitrogen gas at −80 °C. Microfluidic flow chambers were prepared by sandwiching biotin-PEG/PEG passivated coverslips and slides with strips of double-sided tape. In a first step, NeutrAvidin (200 μL, 0.1 mg mL^{-1} in 1× PBS supplemented with 3% BSA (w/v)) was flushed into the chamber and incubated for 5 min. The chamber was washed with 1× PBS (1 mL). DNA disk sample (150 μL, 200 pM) was transferred into the chamber and allowed to bind for 15 min. After washing with 1× PBS (1 mL), PD-1-DNA conjugate (150 μL, 900 nM) was flushed into the channel and incubated for 15 min. After washing with 1× PBS (1 mL), gold nanoparticles (200 μL, stock diluted 1:10 in buffer D) were flushed in and incubated for 5 min. After washing with 1× PBS (1 mL), DNA-PAINT imager strand (500 μL, concentrations in Table S12) diluted in imaging buffer were flushed in. Negative DNA disk controls were prepared in a similar approach using DNA strands without the PD-1.

Microscope Setup. The microscope setup was similar to that described in DNA-PAINT Imaging of PD-L1 on DCs. Imaging parameters used in the different experiments and NeNA values are shown in Table S12.

Image Analysis. Raw fluorescence data were subjected to super-resolution reconstruction using the Picasso software package (Latest version available at https://github.com/jungmannlab/picasso).[40] Drift correction was performed with a redundant cross-correlation and gold nanoparticles as fiducials in Picasso Localize. Prior to analysis, localizations were linked allowing a gap size of 3 frames and a maximum diameter of 1 pixel. To determine the number of spots per DNA disk, most of the particles in the sample were first selected by using the Pick similar function in Picasso Render and subsequently saved by selecting the Save picked localizations function. The total number of DNA disk selected for analysis varied between 5000 and 12000. The number of spots per DNA disk was calculated using single-molecule clustering,[47] identifying the number of individual binding sites for each origami. The two varying parameters in the cluster analysis, radius and minimum number of events, were determined based on the localization precision of the measurement and average numbers of events for individual binding sites and were verified using a smaller region of the data set. The radius depends on the localization precision of the data set and can usually be approximated to 1.5 × NeNA (in nm) of the sample and was set between 2.7 and 5 nm. The minimum number of events was determined by selecting single spots on DNA disk using the Pick similar function and the Save picked properties function in Picasso Render and then opening it in Picasso Filter. The n_events were plotted as a histogram and a minimum number of localizations was set accordingly. Further quantification such as determining the percentage of DNA disk with 2 to 6 spots was performed using Origin Pro 2019b (OriginLab corporation).

Surface Plasmon Resonance Measurements. SPR binding experiments were performed on a Biacore 8K instrument (Cytiva). Mouse PD-L1-Fc chimera protein was diluted in 10 mM sodium acetate (pH 5.5) and immobilized on CM3 sensor chip via EDC/NHS chemistry using an amine coupling kit following the manufacturer’s instructions. For all experiments, ∼300−400 RU of PD-L1-Fc was immobilized on the sensor chip. The running buffer consisted of 10 mM HEPES, 150 mM NaCl, 18 mM $MgCl_2$. Monomeric PD-1 protein and PD-1-DNA conjugates were injected at different concentrations starting from 0.0047 μM to 10 μM (3-fold dilution series) at 30 μL min^{-1}. The response was measured over a 120 s injection with a 600 s dissociation period. No regeneration of the surface was required as the sample completely returned to baseline at the end of the cycle. PD-1 DNA disk samples were injected from 0.078 nM to 10 nM (2-fold dilution series) at 5 μL min^{-1}. DNA disk samples were injected for 420 s followed by a dissociation phase of 600 s. At the end of each cycle, the surface was regenerated by spiking with 10 mM HEPES pH 7.4, 50 mM NaCl for 30 s. Full removal of the analyte was confirmed by the baseline level after the regeneration. Bare DNA disk (no PD-1) was used as negative control. For all samples, the final SPR signal responses were obtained after double-referencing. All measurements were done at 25 °C. All binding curves were analyzed using BIAevaluation software. Binding affinities for monovalent PD-1 and PD-1-DNA conjugate were obtained from steady-state fitting of equilibrium-binding curves. Binding constants for PD-1 DNA disk samples were calculated using a global fit algorithm assuming 1:1 Langmuir binding.

Cell Culture. IL-10-secreting mutuDC (IL-10 DC) line was generously gifted by Prof. Hans Acha-Orbea (UNIL, Lausanne, Switzerland) and described previously.[55] DCs were cultured in IMDM Glutamax supplemented with 10% heat inactivated fetal bovine serum (FBS), 50 U mL^{-1} Penicillin, 50 μg mL^{-1} Streptomycin, 10 mM HEPES, 0.075% sodium bicarbonate, and 50 μM β-mercaptoethanol. B16 cells were cultured in DMEM, high glucose, pyruvate, supplemented with 10% FBS, 50 U mL^{-1} Penicillin and 50 μg mL^{-1} Streptomycin. DCs were subcultured by incubation in nonenzymatic buffer composed of 5 mM EDTA in 1× PBS and B16 by incubation in 1× trypsin-EDTA medium. Cells were grown at 37 °C and 5% CO_2 in a humidified incubator.

Confocal Microscopy Imaging. *Slide Preparation.* DCs were seeded at density of 3×10^4 cells per well in 12-well chamber slides and activated with 200 nM CpG and 100 U mL^{-1} IFNγ for ∼16 h. Cells were fixed in 2% PFA (1:2 dilution in cell media) for 2 min at RT followed by incubation in 4% PFA for 10 min at RT. Nucleus staining was performed with 3 nM DAPI in PBS for 10 min at RT. For DNA disk staining, fixed cells were incubated with a blocking solution (5% normal rat serum (NRS) and purified antimouse CD16/32 antibody (1:100) in PBS) for 1.5 h at RT. Subsequently, cells were blocked with 5 nM bare DNA disks (no dye, no PD-1) for 20 min at 4 °C to minimize nonspecific sticking of DNA disk staining reagents. Blocking steps did not interfere with receptors availability to bind (Figure S19). After blocking, cells were stained with 5 nM DNA origami disk samples for 1 h at RT. For antibody staining, fixed cells were blocked with 5% goat serum for 1.5 h at RT before incubation with primary antibodies (purified antimouse PD-L1 and purified antimouse PD-L2) for 1 h at RT. Antibody detection was performed using Alexa Fluor 647 antibody. ProLong Glass mounting media was used to mount the samples.

Microscope Setup. Images were acquired on a Sp8 confocal microscope (Leica) in an upright configuration with an HC PL APO 20×/0.8 N.A. air objective (Leica). Each image was acquired using the same acquisition settings across the samples within a single experiment. Images were visualized using LAS-X software (Leica) and processed using Fiji software (ImageJ). The same threshold values were applied to all images taken within a single experiment.

Coating of DNA Disks with K_{10}-PEG_{1K}. DNA origami disk samples were coated with oligolysine-PEG copolymer, K_{10}-PEG_{1K}.[51] DNA disk samples were mixed with a solution of K_{10}-PEG_{1K} in a 10:1 volume ratio using a N:P (nitrogen:phosphate) ratio of 1. The mixture was incubated for at least 30 min at RT before use. PEG coating was assessed by AGE (1% agarose, 0.5× TBE, 8 mM $MgCl_2$, 1× SYBR Safe). The gel was run at 70 V for 90 min (Figure S20).

Antibody-DNA Disk Preparation and Purification. PD-L1-DNA conjugates were prepared by incubating mouse anti-PD-L1 antibody (1 mg mL^{-1}) with 4-molar excess NHS-DBCO linker in 20 mM HEPES pH 8, 150 mM NaCl for 4 h at 4 °C with gentle agitation (Figure S21a). Nonreactive NHS-DBCO was removed using 7K MWCO Zeba Spin Desalting columns. Resulting anti-PD-L1-DBCO was reacted with excess azide-ssDNA for ∼16 h at 4 °C with gently agitation. Excess azide-ssDNA was removed using 50k MWCO Amicon Ultra centrifugal filter device precoated with 5% Pluronic F-127 (w/v). The sample was washed repeatedly until no azide-ssDNA was detected in the flowthrough as measured by UV absorption at 260 nm. The concentration of anti-PD-L1-DNA conjugate was determined using a Micro BCA assay kit following manufacturer's instructions. Conjugation efficiency was evaluated by reducing SDS- and native PAGE with Coomassie Blue staining (Figure S21b-c). The conjugates were stored at 4 °C until further use. Ab DNA disk samples were prepared as described above (Figure S22a). Excess anti-PD-L1-DNA conjugates were removed using PEG precipitation protocol (Figure S22b). The number of PEG precipitation rounds was optimized, and presence of antibody in the supernatants was analyzed by SDS-PAGE gel stained with SYPRO Ruby for higher resolution (Figure S22c). The functionalization efficiency of Ab DNA disk was assessed similarly as for PD-1 DNA samples by AGE (Figure S23).

DC Staining Experiments by Flow Cytometry. DCs were seeded at 5×10^4 cells per well in round-bottom 96-well tissue culture plates and stimulated with 200 nM CpG and 100 U mL^{-1} IFNγ for ∼24 h at 37 °C. After stimulation, cells were harvested and incubated with a blocking solution (5% NRS and purified antimouse CD16/32 antibody in stain buffer) for 20 min at 4 °C. Cells were then incubated with 10 nM bare DNA disks (no dye, no PD-1) for 20 min at 4 °C. Surface staining was performed using 5 nM of coated Cy5-integrated DNA disk samples for 30−45 min at 4 °C. To verify activation and PD-L1/PD-L2 surface expression before and after stimulation, cells were stained with control antibody using PE-Cy7 antimouse PD-L1, BV421 antimouse PD-L2 and PE antimouse CD40 antibodies. To test the specificity of binding, cells were blocked with 100 nM anti-PD-L1 and anti-PD-L2 antibodies for 10 min prior staining with DNA disk samples. Cells were analyzed on a LSR Fortessa analyzer (BD Biosciences) using FACSDiva software (BD Biosciences). The acquired data were analyzed using FlowJo software (Tree Star). For flow cytometric imaging, cells were prepared as described above and then acquired on the Amnis ImageStreamX Mark II (Merck Millipore) and analyzed with IDEAS software.

Mice. Female OT-I TCR transgenic mice (C57BL/6-Tg-(TcraTcrb)1100Mjb/Crl) were purchased from Charles River (France). Mice were housed in the EPFL Center of PhenoGenomics (CPG) animal facility. Animal husbandry and euthanasia for spleen and lymph nodes (LNs) extraction were conducted under protocols approved by the veterinary authorities of the Canton de Vaud according to the Swiss regulations (protocol VD3646a). Mice between 7 to 13 weeks of age were used for T cell isolation.

T Cell Isolation. Mouse splenocytes and lymphocytes were extracted by mashing spleen and LNs through a 40 μm cell strainer. Primary OT-I CD8α^+ T cells were subsequently isolated using the EasySep mouse CD8$^+$ T cell isolation kit, following manufacturer's instructions. Until further use, pure CD8α^+ T cells were kept in T cell medium (RPMI-GlutaMAX supplemented with 10% heat-inactivated FBS, 50 U mL^{-1} penicillin, 50 μg mL^{-1} streptomycin, 10 mM HEPES, and 50 μM β-mercaptoethanol) at 4 °C. The purity of isolated CD8α^+ T cells was assessed in LSRII SORP flow cytometry (BD Biosciences). To this end, CD8α^+ T cells were stained with FITC antimouse CD3, PE-Cy5.5 antimouse CD8α, and Fixable Viability Dye eFluor 780. The purity was typically higher than 90% (Figure S12a). Data processing was performed using FACS Diva and FlowJo.

Cell Preparation for Immune Checkpoint Blockade Assay. *DCs and B16.* To induce PD-L1/PD-L2 expression, DCs and B16 (2′500 cells per well) were seeded in round-bottom 96-well tissue culture plates and were stimulated with 100 U mL^{-1} IFNγ and 200 nM CpG (DCs) or 100 U mL^{-1} (B16) for ∼24 h at 37 °C. After ∼21 h of activation, cells were pulsed with 1 nM SIITFEKL peptide for ∼3 h. To characterize the expression of PD-L1, PD-L2 and CD80, nonactivated and stimulated cells were stained with PE-Cy7 antimouse PD-L1, BV421 antimouse PD-L2 and PE-Cy5 antimouse CD80 antibodies. Cells were analyzed by Fortessa flow cytometry and data processed using FACS Diva and FlowJo (Figures S11 and S16).

OT-I T Cells. To induce PD-1 expression, freshly isolated OT-I T cells were stimulated with purified anti-CD3 and anti-CD28 antibodies. More precisely, high-binding 96-well plates were coated with 1 μg mL^{-1} anti-CD3 and 2 μg mL^{-1} anti-CD28 antibodies in PBS overnight at 4 °C. Freshly isolated OT-I T cells were then seeded at ∼6×10^4 cells per well and stimulated for ∼24 h at 37 °C and 5% CO_2 in a humidified incubator. Cells were harvested and rested in T cell medium supplemented with 10 ng mL^{-1} IL-7 for ∼24 h in a 96-well round-bottom plate. To assess activation and PD-1 expression, freshly isolated and stimulated OT-I T cells were stained with FITC anti-PD-1, APC anti-CD8α, PE anti-CD3, eFluor 450 anti-CD25 and Fixable Viability Dye eFluor 780. Cells were analyzed by BD SORP flow cytometry and data processed using FACS Diva and FlowJo (Figure S12b).

***In Vitro* Immune Checkpoint Blockade Assay.** After stimulation, DCs and B16 cells were washed with their respective medium and incubated with blocking reagents (100 nM for control αPD-L1/αPD-L2 antibodies or 5 nM for DNA disk samples) for 45 min prior to coculture with OT-I T cells. Control antibodies were first buffer exchanged with 7K MWCO Zeba Spin Desalting Columns into cell medium to remove sodium azide traces. DNA disk samples were prepared and coated with K_{10}-PEG_{1K} as described earlier. PD-1-expressing OT-I T cells (12′500 cells per well) were cocultured with target cells in DC or B16 medium supplemented with 50 μg mL^{-1} Primocin. After ∼4 h coculture, cell media were replenished with 100 nM control antibodies or 5 nM DNA disk samples. Supernatants were collected after ∼24 h culture and stored at −20 °C for cytokine quantification. IFNγ, TNFα and IL-2 production was measured using commercial Mouse ELISA kits, according to manufacturer's instructions.

Statistical Analysis. Data were presented as mean ± standard deviation (SD) for Figure 1e and mean ± standard error of the mean (SEM) for Figure 3b, 4c, and 5b. The number of replicates for each experiment and the statistical analysis that was performed is specified in the corresponding legend. Data was first tested for normality and subsequently with a parametric or nonparametric test. GraphPad Prism was used for analyses. A p-value less than 0.05 was considered statistically significant among the groups. The p-values were presented as *, **, and *** for $p < 0.05$, $p < 0.01$, and $p < 0.001$, respectively.

ASSOCIATED CONTENT

Supporting Information

The Supporting Information is available free of charge at https://pubs.acs.org/doi/10.1021/acsnano.3c06552.

> PD-L1 density on DCs measured by DNA-PAINT; DNA origami designs and characterization by AGE; PD-1-DNA conjugate characterization by PAGE; AGE analysis of PD-1 DNA disks; DNA-PAINT overview images of hexavalent PD-1 DNA disk pattern library and controls; SPR binding sensorgrams of PD-1 and PD-1-DNA conjugate; control DC staining experiments for PD-1 DNA disks and antibody DNA disks; characterization of immune markers on WT DC, IL-10 DC, and B16 by flow cytometry; additional data on cytokine production in immune checkpoint blockade assay; PD-1 and SrtA purification data; K_{10}-PEG_{1K} DNA disk coating characterization by AGE; sequences for DNA origami disk constructs used in this work; imaging parameters used in DNA-PAINT experiments (PDF)

AUTHOR INFORMATION

Corresponding Author

Maartje M. C. Bastings − *Programmable Biomaterials Laboratory, Institute of Materials, School of Engineering, École Polytechnique Fédérale de Lausanne, Lausanne 1015, Switzerland; Interfaculty Bioengineering Institute, School of Engineering, École Polytechnique Fédérale de Lausanne, Lausanne 1015, Switzerland;* orcid.org/0000-0002-7603-4018; Email: maartje.bastings@epfl.ch

Authors

Kaltrina Paloja − *Programmable Biomaterials Laboratory, Institute of Materials, School of Engineering, École Polytechnique Fédérale de Lausanne, Lausanne 1015, Switzerland;* orcid.org/0000-0001-8504-9919

Jorieke Weiden − *Programmable Biomaterials Laboratory, Institute of Materials, School of Engineering, École Polytechnique Fédérale de Lausanne, Lausanne 1015, Switzerland;* orcid.org/0000-0002-2485-0590

Joschka Hellmeier − *Max Planck Institute of Biochemistry, Planegg 82152, Germany;* orcid.org/0000-0002-7153-9121

Alexandra S. Eklund − *Max Planck Institute of Biochemistry, Planegg 82152, Germany;* orcid.org/0000-0003-1047-2100

Susanne C. M. Reinhardt − *Max Planck Institute of Biochemistry, Planegg 82152, Germany; Faculty of Physics and Center for Nanoscience, Ludwig Maximilian University, Munich 80539, Germany;* orcid.org/0000-0003-0177-4801

Ian A. Parish − *Peter MacCallum Cancer Centre, Melbourne, VIC 3000, Australia; Sir Peter MacCallum Department of Oncology, University of Melbourne, Melbourne, VIC 3128, Australia*

Ralf Jungmann − *Max Planck Institute of Biochemistry, Planegg 82152, Germany; Faculty of Physics and Center for Nanoscience, Ludwig Maximilian University, Munich 80539, Germany;* orcid.org/0000-0003-4607-3312

Complete contact information is available at: https://pubs.acs.org/10.1021/acsnano.3c06552

Author Contributions

¶K.P. and J.W. contributed equally to this work.

Funding

This work was supported by the Human Frontier Science Program (HFSP) through the Young Investigator Grant RGY0065/2018 (M.M.C.B., R.J., I.A.P.), by the Swiss National Science Foundation (SNSF) by Eccellenza grant PCEGP2_181137 (M.M.C.B.), and by a Niels Stensen Fellowship (J.W.).

Notes

The authors declare no competing financial interest.

ACKNOWLEDGMENTS

We thank Prof. Bruno E. Correia for scientific discussion, the Protein Production and Structure Core Facility (PTPSP, EPFL, Switzerland) for performing the PD-1 expression in HEK293 cells, the Flow Cytometry Facility (University of Lausanne, Switzerland) for their help with ImageStream flow cytometry, the Flow Cytometry Core Facility (EPFL, Lausanne) and the BioImaging & Optics Core Facility (EPFL, Lausanne) for providing access to their instruments, and the Center of Phenogenomics (CPG, EPFL, Switzerland) for housing the animals. We furthermore thank Christine Lavanchy for technical assistance, and Prof. Hans Acha-Orbea and Dr. Marianna Koga for providing the mutuDCs.

REFERENCES

(1) Sharpe, A. H.; Pauken, K. E. The Diverse Functions of the PD1 Inhibitory Pathway. *Nat. Rev. Immunol* **2018**, *18* (3), 153−167.

(2) Chikuma, S. Basics of PD-1 in Self-Tolerance, Infection, and Cancer Immunity. *Int. J. Clin Oncol* **2016**, *21* (3), 448−455.

(3) Ceeraz, S.; Nowak, E. C.; Noelle, R. J. B7 Family Checkpoint Regulators in Immune Regulation and Disease. *Trends in Immunology* **2013**, *34* (11), 556−563.

(4) Francisco, L. M.; Sage, P. T.; Sharpe, A. H. The PD-1 Pathway in Tolerance and Autoimmunity. *Immunol Rev.* **2010**, *236*, 219−242.

(5) Cha, J.-H.; Chan, L.-C.; Li, C.-W.; Hsu, J. L.; Hung, M.-C. Mechanisms Controlling PD-L1 Expression in Cancer. *Mol. Cell* **2019**, *76* (3), 359−370.

(6) Juneja, V. R.; McGuire, K. A.; Manguso, R. T.; LaFleur, M. W.; Collins, N.; Haining, W. N.; Freeman, G. J.; Sharpe, A. H. PD-L1 on Tumor Cells Is Sufficient for Immune Evasion in Immunogenic Tumors and Inhibits CD8 T Cell Cytotoxicity. *J. Exp Med.* **2017**, *214* (4), 895−904.

(7) Jiang, X.; Wang, J.; Deng, X.; Xiong, F.; Ge, J.; Xiang, B.; Wu, X.; Ma, J.; Zhou, M.; Li, X.; Li, Y.; Li, G.; Xiong, W.; Guo, C.; Zeng, Z. Role of the Tumor Microenvironment in PD-L1/PD-1-Mediated Tumor Immune Escape. *Molecular Cancer* **2019**, *18* (1), 10.

(8) Page, D. B.; Postow, M. A.; Callahan, M. K.; Allison, J. P.; Wolchok, J. D. Immune Modulation in Cancer with Antibodies. *Annual Review of Medicine* **2014**, *65* (1), 185−202.

(9) Acúrcio, R. C.; Pozzi, S.; Carreira, B.; Pojo, M.; Gómez-Cebrián, N.; Casimiro, S.; Fernandes, A.; Barateiro, A.; Farricha, V.; Brito, J.; Leandro, A. P.; Salvador, J. A. R.; Graça, L.; Puchades-Carrasco, L.; Costa, L.; Satchi-Fainaro, R.; Guedes, R. C.; Florindo, H. F.

Therapeutic Targeting of PD-1/PD-L1 Blockade by Novel Small-Molecule Inhibitors Recruits Cytotoxic T Cells into Solid Tumor Microenvironment. *J. Immunother Cancer* **2022**, *10* (7), No. e004695.

(10) Yang, J.; Hu, L. Immunomodulators Targeting the PD-1/PD-L1 Protein-Protein Interaction: From Antibodies to Small Molecules. *Medicinal Research Reviews* **2019**, *39* (1), 265−301.

(11) Guo, L.; Wei, R.; Lin, Y.; Kwok, H. F. Clinical and Recent Patents Applications of PD-1/PD-L1 Targeting Immunotherapy in Cancer Treatment—Current Progress, Strategy, and Future Perspective. *Front. Immunol.* **2020**, DOI: 10.3389/fimmu.2020.01508.

(12) Day, D.; Hansen, A. R. Immune-Related Adverse Events Associated with Immune Checkpoint Inhibitors. *BioDrugs* **2016**, *30* (6), 571−584.

(13) Xu-Monette, Z. Y.; Zhang, M.; Li, J.; Young, K. H. PD-1/PD-L1 Blockade: Have We Found the Key to Unleash the Antitumor Immune Response? *Front. Immunol.* **2017**, DOI: 10.3389/fimmu.2017.01597.

(14) Wang, Z.; Wu, X. Study and Analysis of Antitumor Resistance Mechanism of PD1/PD-L1 Immune Checkpoint Blocker. *Cancer Medicine* **2020**, *9* (21), 8086−8121.

(15) Sun, J.-Y.; Zhang, D.; Wu, S.; Xu, M.; Zhou, X.; Lu, X.-J.; Ji, J. Resistance to PD-1/PD-L1 Blockade Cancer Immunotherapy: Mechanisms, Predictive Factors, and Future Perspectives. *Biomark Res.* **2020**, *8*, 35.

(16) Dustin, M. L.; Tseng, S.-Y.; Varma, R.; Campi, G. T Cell−Dendritic Cell Immunological Synapses. *Current Opinion in Immunology* **2006**, *18* (4), 512−516.

(17) Dustin, M. L.; Chakraborty, A. K.; Shaw, A. S. Understanding the Structure and Function of the Immunological Synapse. *Cold Spring Harb Perspect Biol.* **2010**, *2* (10), No. a002311.

(18) Sallusto, F.; Lanzavecchia, A. The Instructive Role of Dendritic Cells on T-Cell Responses. *Arthritis Res.* **2002**, *4* (Suppl 3), S127−S132.

(19) Doh, J.; Irvine, D. J. Immunological Synapse Arrays: Patterned Protein Surfaces That Modulate Immunological Synapse Structure Formation in T Cells. *Proc. Natl. Acad. Sci. U.S.A.* **2006**, *103* (15), 5700−5705.

(20) Oh, S. A.; Wu, D.-C.; Cheung, J.; Navarro, A.; Xiong, H.; Cubas, R.; Totpal, K.; Chiu, H.; Wu, Y.; Comps-Agrar, L.; Leader, A. M.; Merad, M.; Roose-Germa, M.; Warming, S.; Yan, M.; Kim, J. M.; Rutz, S.; Mellman, I. PD-L1 Expression by Dendritic Cells Is a Key Regulator of T-Cell Immunity in Cancer. *Nat. Cancer* **2020**, *1* (7), 681−691.

(21) Yokosuka, T.; Takamatsu, M.; Kobayashi-Imanishi, W.; Hashimoto-Tane, A.; Azuma, M.; Saito, T. Programmed Cell Death 1 Forms Negative Costimulatory Microclusters That Directly Inhibit T Cell Receptor Signaling by Recruiting Phosphatase SHP2. *J. Exp Med.* **2012**, *209* (6), 1201−1217.

(22) Pentcheva-Hoang, T.; Chen, L.; Pardoll, D. M.; Allison, J. P. Programmed Death-1 Concentration at the Immunological Synapse Is Determined by Ligand Affinity and Availability. *Proc. Natl. Acad. Sci. U. S. A.* **2007**, *104* (45), 17765−17770.

(23) Fang, T.; Alvelid, J.; Spratt, J.; Ambrosetti, E.; Testa, I.; Teixeira, A. I. Spatial Regulation of T-Cell Signaling by Programmed Death-Ligand 1 on Wireframe DNA Origami Flat Sheets. *ACS Nano* **2021**, *15* (2), 3441−3452.

(24) Ruglioni, M.; Civita, S.; Salvadori, T.; Cristiani, S.; Carnicelli, V.; Barachini, S.; Petrini, I.; Diaspro, A.; Bianchini, P.; Storti, B.; Bizzarri, R.; Fogli, S.; Danesi, R. Nanoscale Engagement of Immune Checkpoint Inhibitor PD-L1 in Membrane Lipid Rafts. *bioRxiv*, August 11, 2022. DOI: 10.1101/2022.08.09.503318.

(25) Zhou, L.; Chai, F.; He, Y.; Zhou, Z.; Guo, S.; Li, P.; Sun, Q.; Zu, X.; Liu, X.; Huang, Q.; Zhong, Y.; Zhou, A.; Wang, X.; Ren, H. Homodimerized Cytoplasmic Domain of PD-L1 Regulates Its Complex Glycosylation in Living Cells. *Commun. Biol.* **2022**, *5* (1), 1−12.

(26) Rothemund, P. W. K. Folding DNA to Create Nanoscale Shapes and Patterns. *Nature* **2006**, *440* (7082), 297−302.

(27) Seeman, N. C.; Sleiman, H. F. DNA Nanotechnology. *Nat. Rev. Mater.* **2018**, *3* (1), No. 17068.

(28) Zhan, P.; Peil, A.; Jiang, Q.; Wang, D.; Mousavi, S.; Xiong, Q.; Shen, Q.; Shang, Y.; Ding, B.; Lin, C.; Ke, Y.; Liu, N. Recent Advances in DNA Origami-Engineered Nanomaterials and Applications. *Chem. Rev.* **2023**, *123* (7), 3976−4050.

(29) Comberlato, A.; Koga, M. M.; Nüssing, S.; Parish, I. A.; Bastings, M. M. C. Spatially Controlled Activation of Toll-like Receptor 9 with DNA-Based Nanomaterials. *Nano Lett.* **2022**, *22* (6), 2506−2513.

(30) Kurisinkal, E. E.; Caroprese, V.; Koga, M. M.; Morzy, D.; Bastings, M. M. C. Selective Integrin A5β1 Targeting through Spatially Constrained Multivalent DNA-Based Nanoparticles. *Molecules* **2022**, *27* (15), 4968.

(31) Hellmeier, J.; Platzer, R.; Eklund, A. S.; Schlichthaerle, T.; Karner, A.; Motsch, V.; Schneider, M. C.; Kurz, E.; Bamieh, V.; Brameshuber, M.; Preiner, J.; Jungmann, R.; Stockinger, H.; Schütz, G. J.; Huppa, J. B.; Sevcsik, E. DNA Origami Demonstrate the Unique Stimulatory Power of Single PMHCs as T Cell Antigens. *Proc. Natl. Acad. Sci. U. S. A.* **2021**, *118* (4), No. e2016857118.

(32) Shaw, A.; Lundin, V.; Petrova, E.; Fördős, F.; Benson, E.; Al-Amin, A.; Herland, A.; Blokzijl, A.; Högberg, B.; Teixeira, A. I. Spatial Control of Membrane Receptor Function Using Ligand Nanocalipers. *Nat. Methods* **2014**, *11* (8), 841−846.

(33) Veneziano, R.; Moyer, T. J.; Stone, M. B.; Wamhoff, E.-C.; Read, B. J.; Mukherjee, S.; Shepherd, T. R.; Das, J.; Schief, W. R.; Irvine, D. J.; Bathe, M. Role of Nanoscale Antigen Organization on B-Cell Activation Probed Using DNA Origami. *Nat. Nanotechnol.* **2020**, *15* (8), 716−723.

(34) Berger, R. M. L.; Weck, J. M.; Kempe, S. M.; Hill, O.; Liedl, T.; Rädler, J. O.; Monzel, C.; Heuer-Jungemann, A. Nanoscale FasL Organization on DNA Origami to Decipher Apoptosis Signal Activation in Cells. *Small* **2021**, *17* (26), No. 2101678.

(35) Bila, H.; Kurisinkal, E. E.; Bastings, M. M. C. Engineering a Stable Future for DNA-Origami as a Biomaterial. *Biomaterials Science* **2019**, *7*, 532.

(36) Koga, M. M.; Comberlato, A.; Rodríguez-Franco, H. J.; Bastings, M. M. C. Strategic Insights into Engineering Parameters Affecting Cell Type-Specific Uptake of DNA-Based Nanomaterials. *Biomacromolecules* **2022**, *23* (6), 2586−2594.

(37) Rodríguez-Franco, H. J.; Weiden, J.; Bastings, M. M. C. Stabilizing Polymer Coatings Alter the Protein Corona of DNA Origami and Can Be Engineered to Bias the Cellular Uptake. *ACS Polym. Au* **2023**, *3*, No. 344.

(38) Peng, Q.; Qiu, X.; Zhang, Z.; Zhang, S.; Zhang, Y.; Liang, Y.; Guo, J.; Peng, H.; Chen, M.; Fu, Y.-X.; Tang, H. PD-L1 on Dendritic Cells Attenuates T Cell Activation and Regulates Response to Immune Checkpoint Blockade. *Nat. Commun.* **2020**, *11* (1), 4835.

(39) Jungmann, R.; Steinhauer, C.; Scheible, M.; Kuzyk, A.; Tinnefeld, P.; Simmel, F. C. Single-Molecule Kinetics and Super-Resolution Microscopy by Fluorescence Imaging of Transient Binding on DNA Origami. *Nano Lett.* **2010**, *10* (11), 4756−4761.

(40) Schnitzbauer, J.; Strauss, M. T.; Schlichthaerle, T.; Schueder, F.; Jungmann, R. Super-Resolution Microscopy with DNA-PAINT. *Nat. Protoc.* **2017**, *12* (6), 1198−1228.

(41) Eklund, A. S.; Comberlato, A.; Parish, I. A.; Jungmann, R.; Bastings, M. M. C. Quantification of Strand Accessibility in Biostable DNA Origami with Single-Staple Resolution. *ACS Nano* **2021**, *15* (11), 17668−17677.

(42) Vanamee, É. S.; Faustman, D. L. Structural Principles of Tumor Necrosis Factor Superfamily Signaling. *Science Signaling* **2018**, *11* (511), No. eaao4910.

(43) Kwon, P. S.; Ren, S.; Kwon, S.-J.; Kizer, M. E.; Kuo, L.; Xie, M.; Zhu, D.; Zhou, F.; Zhang, F.; Kim, D.; Fraser, K.; Kramer, L. D.; Seeman, N. C.; Dordick, J. S.; Linhardt, R. J.; Chao, J.; Wang, X. Designer DNA Architecture Offers Precise and Multivalent Spatial Pattern-Recognition for Viral Sensing and Inhibition. *Nat. Chem.* **2020**, *12* (1), 26−35.

(44) Castro, M.; van Santen, H. M.; Férez, M.; Alarcón, B.; Lythe, G.; Molina-París, C. Receptor Pre-Clustering and T Cell Responses: Insights into Molecular Mechanisms. *Front. Immunol.* **2014**, DOI: 10.3389/fimmu.2014.00132.

(45) Parker, K.; Trampert, P.; Tinnemann, V.; Peckys, D.; Dahmen, T.; de Jonge, N. Linear Chains of HER2 Receptors Found in the Plasma Membrane Using Liquid-Phase Electron Microscopy. *Biophys. J.* **2018**, *115* (3), 503−513.

(46) Bila, H.; Paloja, K.; Caroprese, V.; Kononenko, A.; Bastings, M. M. C. Multivalent Pattern Recognition through Control of Nano-Spacing in Low-Valency Super-Selective Materials. *J. Am. Chem. Soc.* **2022**, *144* (47), 21576−21586.

(47) Reinhardt, S. C. M.; Masullo, L. A.; Baudrexel, I.; Steen, P. R.; Kowalewski, R.; Eklund, A. S.; Strauss, S.; Unterauer, E. M.; Schlichthaerle, T.; Strauss, M. T.; Klein, C.; Jungmann, R. Ångström-Resolution Fluorescence Microscopy. *Nature* **2023**, *617* (7962), 711−716.

(48) Magnez, R.; Thiroux, B.; Taront, S.; Segaoula, Z.; Quesnel, B.; Thuru, X. PD-1/PD-L1 Binding Studies Using Microscale Thermophoresis. *Sci. Rep* **2017**, *7* (1), No. 17623.

(49) Lázár-Molnár, E.; Scandiuzzi, L.; Basu, I.; Quinn, T.; Sylvestre, E.; Palmieri, E.; Ramagopal, U. A.; Nathenson, S. G.; Guha, C.; Almo, S. C. Structure-Guided Development of a High-Affinity Human Programmed Cell Death-1: Implications for Tumor Immunotherapy. *EBioMedicine* **2017**, *17*, 30−44.

(50) Butte, M. J.; Keir, M. E.; Phamduy, T. B.; Sharpe, A. H.; Freeman, G. J. Programmed Death-1 Ligand 1 Interacts Specifically with the B7−1 Costimulatory Molecule to Inhibit T Cell Responses. *Immunity* **2007**, *27* (1), 111−122.

(51) Ponnuswamy, N.; Bastings, M. M. C.; Nathwani, B.; Ryu, J. H.; Chou, L. Y. T.; Vinther, M.; Li, W. A.; Anastassacos, F. M.; Mooney, D. J.; Shih, W. M. Oligolysine-Based Coating Protects DNA Nanostructures from Low-Salt Denaturation and Nuclease Degradation. *Nat. Commun.* **2017**, *8* (1), No. 15654.

(52) Ueno, H.; Klechevsky, E.; Morita, R.; Aspord, C.; Cao, T.; Matsui, T.; Di Pucchio, T.; Connolly, J.; Fay, J. W.; Pascual, V.; Palucka, A. K.; Banchereau, J. Dendritic Cell Subsets in Health and Disease. *Immunological Reviews* **2007**, *219* (1), 118−142.

(53) Domogalla, M. P.; Rostan, P. V.; Raker, V. K.; Steinbrink, K. Tolerance through Education: How Tolerogenic Dendritic Cells Shape Immunity. *Front. Immunol.* **2017**, DOI: 10.3389/fimmu.2017.01764.

(54) Iberg, C. A.; Hawiger, D. Natural and Induced Tolerogenic Dendritic Cells. *J. Immunol.* **2020**, *204* (4), 733−744.

(55) Koga, M. M.; Engel, A.; Pigni, M.; Lavanchy, C.; Stevanin, M.; Laversenne, V.; Schneider, B. L.; Acha-Orbea, H. IL10- and IL35-Secreting MutuDC Lines Act in Cooperation to Inhibit Memory T Cell Activation Through LAG-3 Expression. *Front. Immunol.* **2021**, DOI: 10.3389/fimmu.2021.607315.

(56) Zhao, Y.; Lee, C. K.; Lin, C.-H.; Gassen, R. B.; Xu, X.; Huang, Z.; Xiao, C.; Bonorino, C.; Lu, L.-F.; Bui, J. D.; Hui, E. PD-L1:CD80 Cis-Heterodimer Triggers the Co-Stimulatory Receptor CD28 While Repressing the Inhibitory PD-1 and CTLA-4 Pathways. *Immunity* **2019**, *51* (6), 1059−1073.

(57) Sansom, D. M.; Walker, L. S. K. Dimers Aren't Forever: CD80 Breaks up with PD-L1. *Immunity* **2019**, *51* (6), 972−974.

(58) Martinez-Veracoechea, F. J.; Frenkel, D. Designing Super Selectivity in Multivalent Nano-Particle Binding. *Proc. Natl. Acad. Sci. U. S. A.* **2011**, *108* (27), 10963−10968.

(59) Curk, T.; Dobnikar, J.; Frenkel, D. Optimal Multivalent Targeting of Membranes with Many Distinct Receptors. *Proc. Natl. Acad. Sci. U. S. A.* **2017**, *114* (28), 7210−7215.

(60) Dubacheva, G. V.; Curk, T.; Richter, R. P. Determinants of Superselectivity—Practical Concepts for Application in Biology and Medicine. *Acc. Chem. Res.* **2023**, *56* (7), 729−739.

(61) Strauss, S.; Jungmann, R. Up to 100-Fold Speed-up and Multiplexing in Optimized DNA-PAINT. *Nat. Methods* **2020**, *17* (8), 789−791.

(62) Fabricius, V.; Lefèbre, J.; Geertsema, H.; Marino, S. F.; Ewers, H. Rapid and Efficient C-Terminal Labeling of Nanobodies for DNA-PAINT. *J. Phys. D: Appl. Phys.* **2018**, *51* (47), No. 474005.

(63) Eklund, A. S.; Ganji, M.; Gavins, G.; Seitz, O.; Jungmann, R. Peptide-PAINT Super-Resolution Imaging Using Transient Coiled Coil Interactions. *Nano Lett.* **2020**, *20* (9), 6732−6737.